Core flow cooling rig design and CFD database report

ENABLE·H2

ENABLing cryogEnic Hydrogen-based CO2-free air transport

Call identifier

H2020-MG-2016-2017/H2020-MG-2017-Two-Stages

Project start

01.09.2018

Project duration

51 months

ENABLEH2

D2.2 - Core flow cooling rig design and CFD database report

Authors: Isak Jonsson, Alexandre Capitao Patrao, Carlos Xisto
Deliverable lead beneficiary: Chalmers

Executive summary
This report provides a detailed description of the design, construction, and commissioning of the new 2.5-stage low-pressure compressor test facility at Chalmers Laboratory of Fluids and Thermal Sciences. The facility was commissioned as part of the ENABLEH2 project for detailed heat-transfer studies on compressor turbomachinery. The generated experimental data is used for validation of the numerically predicted aerothermal performance at the intermediate compressor duct. Results are presented and benchmarked against verification data from detailed multi-hole probe, hot-wire anemometry, Kiel probe, pressure taps and surface heat transfer measurements. The facility's performance and provided experimental verification data is of high resolution, high stability, and flow uniformity.

Table of Content

1 Glossary

Abbreviation	Description
5HP	Five-hole probe
ADP	At Design Point
CFD	Computational Fluid Dynamics
CNC	Computer Numerical Control
GPS	Geometrical Product Specifications
HEX	Heat Exchanger
HTR	Hub-to-tip
ICD	Intermediate Compressor Duct
IGV	Inlet Guide Vane
IR	Infrared
ISO	International Organization for Standardization
LPC	Low-Pressure Compressor
LPT	Low-Pressure Turbine
MCS	Monte Carlo Simulation
MHP	Multi-hole Probe
OGV	Outlet Guide Vanes
PIV	Particle Imaging Velocimetry
PTC	Performance Test Code
RPM	Revolutions Per Minute
RSS	Root Sum Square
RTD	Resistance Temperature Detectors
SLA	Stereolithography
TRS	Turbine Rear Structure
VINK	Virtuell Integrerad Kompressordemonstrator

2 Introduction

As part of work package2 in the European project ENABLEH2, a new low pressure compressor facility was designed and constructed at Chalmers Laboratory of Fluids and Thermal Sciences. The principal purpose of the facility is to experimentally evaluate the intermediate compressor duct's (ICD)ability to synergistically be utilised as a heat exchanger in cryogenic fuelled engine concepts. Thus, the facility is designed to evaluate engine-typical ICDs as well as novel synergistic ICD heat-exchanger concepts. Further information of the ENABLEH2 project heat management targets are presented in the accompanied deliveries 2.1 and 2.4. This report focuses on the design, construction, and commissioning on the new compressor facility and summarizes the CFD results.

The facility is a vertical annular 2.5-stage low-speed compressor rig, built for continuous operation at a wide operational range of Reynolds numbers and pressure ratios. The general layout of the facility can be seen in Figure 2-1 where the two-stage compressor drives the main flow in the facility. Operational conditions are achieved by restricting the flow with a restrictor upstream of the low pressure compressor LPC and regulating the compressor's input power. The flow is conditioned for thermal and pressure uniformity in a combined volute and flow conditioner between the restrictor and the compressor inlet. The ICD is mounted downstream of the two-stage compressor, and the ICD outlet is the outlet of the facility. The flow is recirculated into the facility in the return duct for thermal stability, to limit particle ingestion and for noise damping.
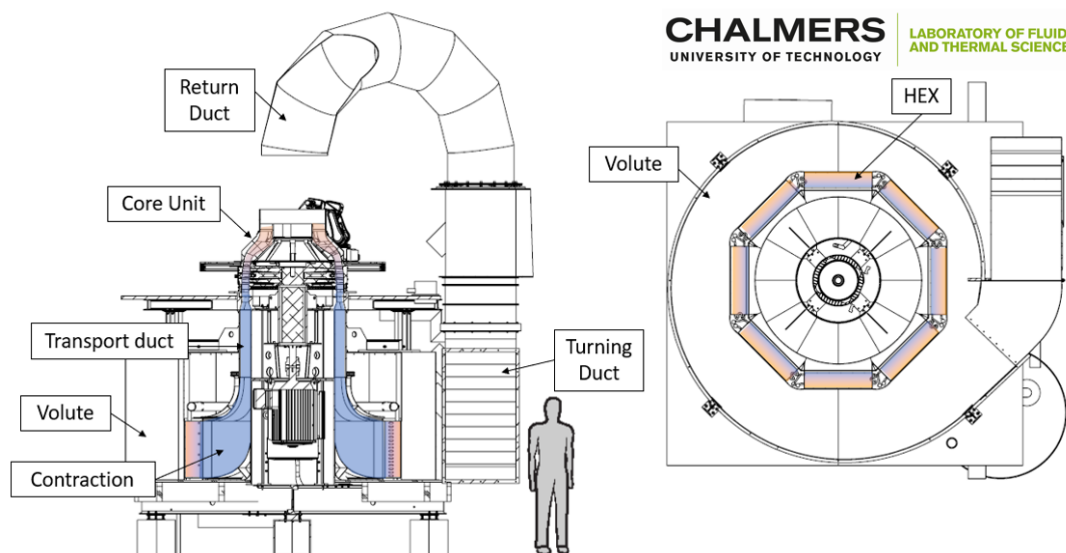

Figure 2-1: Schematics of Chalmers low-pressure compressor facility.

The LPC consists of 75 adjustable inlet guide vanes (IGV), rotor 1 with 61 blades (r1), stator 1 with 124 stator vanes (s1), rotor 2 with 69 blades (r2) and finally, the outlet guide vane (OGV) with 126 vanes. The LPC design is derived from a slightly updated version of the VINK LPC presented in Lejon et al. in [1]. Fundamental aerodynamic and geometrical design similarity was targeted, such as flow, load coefficients, De-Haller number, hub-to-tip ratio, Reynolds Number and tip-clearance. The design was constrained by the physical and power limitations of the lab and available instrumentation. The LPC and ICD designs were iterated with these initial targets and constraints between the experimentalist and the aerodynamic designer. The final aerodynamic design of the LPC was performed at GKN using both in-house design methods and methods similar to those presented in this report. Section 2.2 elaborates on the mechanical and aerodynamic design choices of the LPC.

The facility design can be divided into two groups, of which the first group relates to the core flow components, such as the LPC and the ICD. The secondary group comprises the systems that support the first group, such as mechanical structure, cooling and manufacturability. This report focuses on the first group, and the following section describes the design along the flow path from the inlet to the outlet. The secondary group is briefly covered in the report but is primarily aimed to improve operation, simplify assembly, and enable access to the ICD and compressor. All the compressor parts were designed to have a safety factor above three for a five-year normal operation period. Time allocated for the design of these subsystems was based on the impact of failure from a qualitative risk assessment. Hence, the outer structures were assessed with hand calculations and classic beam correlations due to the low

impact of failure, while structures, such as the LPC mount, were extensively simulated for both dynamic and static loads using the mechanical workbench in Ansys™.

2.1 Design of the flow conditioning unit

The purpose of the flow condition unit is to provide flow of high quality at the required pressure, temperature, and turbulence intensity to the downstream compressor. Industrial jalousie dampeners enable simple control of the mass flow upstream of the LPC. However, the outlet flow from such a device is highly non-uniform and not suitable for the compressor inlet as axial compressors are sensitive to blade flow angles and inlet flow distortions. The propagation of inlet distortions of about 20% in total pressure through several stages of a transonic compressor was investigated by Longley et. al [2]. Even though some damping effects were observed, a substantial part of the distortions propagated through the compressor. Local and large distortions will interfere with performance evaluation, but the effects can be mitigated if the position is known. Random and unsteady inlet distortions are more challenging to compensate for, and a minimal amount of random inlet distortion is preferred. The random inlet distortions are primarily mitigated through the flow conditioner and require detailed considerations. The general outline of the flow conditioning unit is shown in Figure 2-2, where the coloured streamlines of velocity magnitude are seeded from the inlet to illustrate the internal flow path. The flow enters at the inlet and in the azimuthal direction into the volute. The volute maintains a constant azimuthal velocity while the flow is guided radially through eight heat-exchangers (HEX). The HEX serve two purposes; first, they keep the thermal balance in the facility as they are connected to the building central cooling system. Second, the HEX reduces non-uniformity in the flow. The cross-section plane and streamlines illustrate the acceleration from radial to the axial direction in the contraction after the HEX. The contours at the outlet plane follow the same colour scale as the streamlines and cross-section contours in Figure 2-2. The simulation of the flow conditioning unit was performed in STAR-CCM+ and is detailed in [3]. In Figure 2-2, the azimuthal variation of total pressure and velocity at midspan 300 mm downstream of the outlet plane is illustrated below the isometric view of the flow conditioner. At the outlet plane at the midspan, the numerical results indicated variations in total pressure and velocity below $\pm$ 1% of the mean flow, which was considered acceptable.
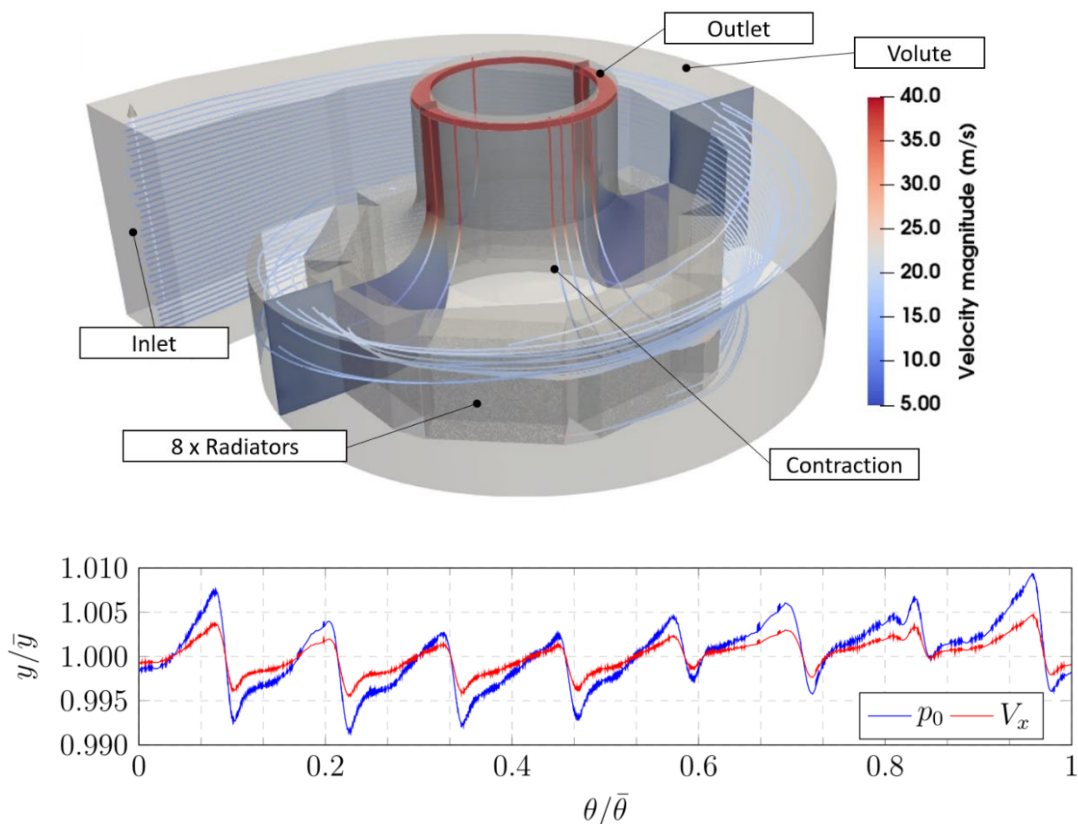

Figure 2-2: Midspan velocity and pressure distribution 300 mm downstream of the contraction outlet (Lower). Spacing of grid lines on the plot represent tangential resolution for inlet condition probe access. The streamlines from the numerical simulation are shown the upper image.

After the contraction, the flow is guided through a transport channel where it passes by structural vanes. The structural vanes are shaped as NACA0018 profiles due to the high bending stiffness to wake width and placed with a 90-degree offset. After the transport channel, the flow is accelerated in a contraction with a contraction ratio of 0.85. Before entering the IGV, a turbulence screen is placed to increase turbulence levels and further reduce residual non-uniformity.

2.2 Design of the compressor unit

This section describes the aerodynamic and mechanical design of the low-pressure compressor and begins by providing the rationale behind some fundamental and practical design parameters.

2.2.1 Reynolds number effects

The operation of a compressor with respect to Reynolds number can be divided into three regimes. First is the lower (also called laminar separation) regime $Re_{crit,L}$. The name is derived from often-occurring laminar separation on the suction side, causing a rapid loss in performance and turning ability, illustrated on the left in Figure 2-3. This ranges from Reynolds number 100,000 as observed by Shäffler [4] to as low as 50,000 as observed by Carter [5]. The upper critical region (also called roughness region) is defined by a relation to surface roughness but can, for most aero-engine representative surfaces, be around 600,000 [4]. In this region, polytropic efficiency is nearly Reynolds number independent as surface features penetrate the sub-layer, as illustrated on the right of Figure 2-3. Between these two regions is where the vast majority of low-speed test rigs operate, with for the most part, an attached turbulent boundary layer. Interoperated in Figure 2-3 is the polytropic efficiency on the vertical axis and rotor chord Reynolds number on the horizontal axis. The trends of polytropic efficiency throughout the three regions are illustrated by a black dashed line for typical values and a blue shaded zone that represents relative ranges in the data set based on previously published reports [4, 5]. In the laminar region, one can note a high Reynolds dependency of the polytropic efficiency. Near the interface of $Re_{crit,L}$ there is little correlation to Reynolds numbers as variations between compressors can influence when the flow translates between a laminar separation to turbulent operation. The lowest acceptable operational point at 3×10^6 Re_c was selected to mitigate the aforementioned undesired operational conditions. The horizontal solid red line in Figure 2-3 represents the facility design operation from a $3 \times 10^6 - 6 \times 10^6$ Re_c with the design point at 5.75×10^6. With this selected operational range, speed-lines down to 0.5 should be possible without any risk of large-scale laminar separation. The facility is capable of being operational down to even lower Reynolds numbers to be able to identify the $Re_{crit,L}$ with some penalty in measurement accuracy. The lower operation region is shown in Figure 2-3 as the horizontal red dashed line.
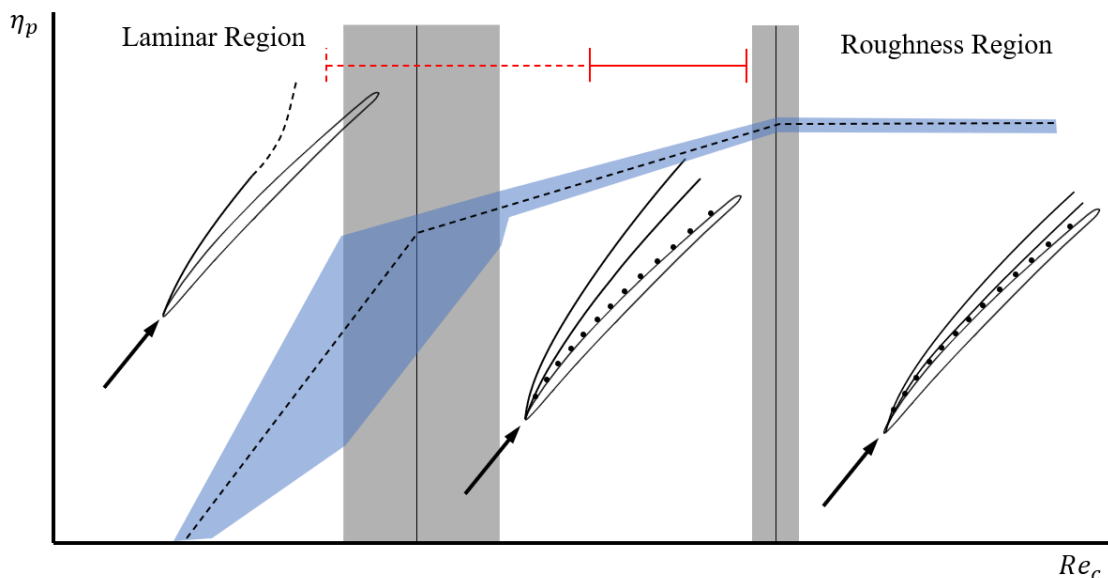
Figure 2-3: Operational regions of a compressor in relation to rotor chord Reynolds number. A schematic boundary layer development relative to surface features for each region together with representative polytropic efficiency (black dashed line), typical ranges in the existing experimental data (blue shaded area) and facility operational range (red horizontal line). The facility is also possible to operate down to the laminar region (red dashed line) with some penalty in measurement accuracy.

2.2.2 Influence of freestream turbulence

Turbulence intensity and length-scale influence the boundary layer development and are known to influence performance in turbomachinery [6]. Hence, a representative level is important to achieve. However, the turbulence intensity can vary substantially in a compressor, so a specific target value is arguably hard to pinpoint. Low-speed facilities are reported to operate in ranges between 3-11% [7]. Data for high-pressure compressor outlets at full speed tests are reported to be in ranges of $6 - 7\%$ in [8]. Mayle [6] investigated the effect of free-stream turbulence on the critical momentum thickness number at higher Reynolds number. His results indicate that the effect from turbulence intensity above $3 - 4\%$ generally subsidies. Numerical simulations on compressor blades from [9] based on transition models of B. Abu-Ghannam and R. Shaw [10] shown in Ref. [11] suggest that at a Reynolds of 5×10^6, any turbulence level above $2 - 3\%$ should have a small effect on the transition onset location. With this in mind, an isotropic turbulence intensity of $3 - 4\%$ at the inlet of the IGV was targeted. The turbulence was achieved using a single turbulence grid upstream of the IGV inlet. For the final design, a turbulence grid with $1mm$ steel wires and a centre gap of $3.15mm$ was selected to achieve 3.75% turbulence intensity at the IGV inlet during design operation. The selection of the screens and calculation of turbulence decay was performed following the guidelines in Ref. [12].

An interesting note is that when Schreiber [11] investigated the combined effects of Reynolds number and turbulence on transition location in a linear cascade, he observed high sensitivity to both turbulence and Reynolds number at around a Re_c of $200,000$ and a turbulence level around 3%. This concurs with earlier presented studies and strengthens the rationale for a lower selected Re_c of $300,000$ and a turbulence intensity of $3 - 4\%$ as this places the facility far upstream of these critical conditions. Another interesting note is that Cyrus [13] showed that increasing the turbulence from 3.8% to 6.2% moved the stall factor towards a lower flow factor for the same load coefficient. The facility where the experiments were performed is similar in Reynolds number, size and rotational speed as the design at Chalmers Laboratory of Fluids and Thermal Sciences.

It is worth noting that discussing turbulence without consideration for length-scale is a gross oversimplification but is arguably sufficient for initial design and general down-selection.

2.2.3 Surface roughness effects

The surface roughness impacts the aerodynamic performance of the LPC. A near hydraulic low surface roughness is preferred to avoid effects from surface roughness, but a smoother surface negatively impacts component price. Therefore, a reasonable level of surface roughness for current operational conditions was required.

From a fluid dynamic perspective, the geometrical sand-grain roughness k_s, sand-grain roughness height $k_{s,h}$ and the dimensionless friction factor f are commonly used. However, in practice, the surface specifications in technical drawings are statistical, as defined by ISO-4287 [14]. An exact conversion from statistical ISO units such as R_a and R_y to geometrical sand grain roughness k_s is a much-debated subject. In Ref. [15], a GKN in-house correlation was used to relate statistical values to surface roughness.

For low-speed compressor test facilities, surface roughness typically affects the boundary layer development and separation location. In simplified two-dimensional conditions, the dependency of surface roughness effects on the boundary layer state can be categorised by the dimensionless surface roughness k_s^+, as defined in Equation 2-1.

$$k_s^+ = \frac{k_s}{\delta_v} \quad \begin{array}{ccc} 0 \le k_s^+ \le 5 & 5 \le k_s^+ \le 70 & 70 \le k_s^+ \\ Smooth & Transitional & Rough \end{array} \qquad \textit{2-1}$$

The effect of the dimensionless surface roughness can be divided into three zones. For values of $k_s^+ < 5$, the surface can be considered hydraulically smooth. At values with a dimensionless roughness parameter above 70, the surface can be considered fully rough as the average fluctuation penetrates the overlap region. In the area between these two, the surface topology has a significant impact on boundary layer development. In this area, the conversion from statistical to equivalent sand-grain roughness is arguably challenging. One empirical model derived from a relatively large dataset of measured surfaces is presented by Flack and Schultz [16] and is defined in Equation 2-2. R_q is the RSS of perturbations, and Rsk is the skewness as defined in ISO-4287 [14]. The skewness provides a

measure of the direction of the surface variations. At a high skewness, the majority of the perturbation extrudes into the flow and vice-versa.

$$k_s = 4.43R_q(1 + Rsk)^{1.37} \qquad \text{2-2}$$

Assuming that the measured surface roughness has been estimated correctly, the surface roughness effect on the laminar-turbulent transition onset location can be estimated using the roughness parameter $\theta_t/k_{s,h}$. This parameter has been empirically correlated to the onset momentum thickness Reynolds number by using Equation 2-3.

$$\text{Re}_{\theta_t} = 100 + 0.43e^{\left(7-0.77\frac{k_{s,h}}{\theta_t}\right)} \qquad \text{2-3}$$

$$\text{Re}_{\theta_t} = 400\text{Tu}^{5/8} \qquad \text{2-4}$$

Equations 2-3 and 2-4 describe the effect from surface roughness and turbulence levels, respectively, and both are illustrated in Figure 2-4. Figure 2-4 shows that for most turbulence levels expected in the LPC $(3\% - 10\%)$, the sand-grain roughness height needs to be in the order of two to five times the size of the momentum thickness (θ) to have an impact on the momentum thickness at transition onset. This method provides a starting point when defining the manufacturing demands on aero surfaces.
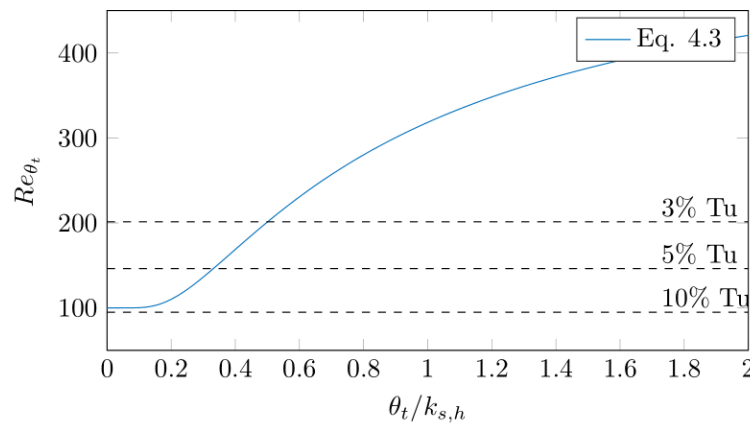

Figure 2-4 Turbulence and surface roughness effects on the transition onset momentum thickness Reynolds number Re_{θ_t}.

With the present design, a rotor blade operating around at design point (ADP) perceives a velocity of $70 - 80$ m/s and an assumed turbulence intensity of 3% at midspan. Equation 2-4 provides an onset momentum thickness Reynolds number, and with ambient conditions, an estimated momentum thickness. Inserting these into Equation 2-3, the maximum allowed sand grain roughness can then be estimated to be $k_s = 16.5\mu m$. In a modern, five-axis, high-speed spindle CNC-mill it is relatively easy to achieve a R_q and Rsk that would result in a sand grain roughness below $k_s = 16.5\mu m$. After discussion with the manufacturers and providing an ample margin for error in the above rationale, a $Rq \leq 2\mu m$ and a near-zero Rsk were targeted.

In terms of surface roughness and geometrical design, local manufacturing defects are present and accepted near the trailing edge on the pressure side. These defects consist of entry and exit paths from the milling finishing procedure.

2.2.4 Compressibility effects

All the experimental and numerical work related to this facility was performed at low Mach numbers. In a real engine, the flow is compressible with an ICD inlet Mach number around $0.4 - 0.6$ and local peaks of $0.8 - 0.9$. Critical features in the ICD are instabilities and stochastic features in the boundary layer, which are challenging to capture numerically and significantly impact heat transfer and duct performance. These features are possible to evaluate at a low Mach number in otherwise representative conditions.

The last two stages in the LPC are typically transonic, which this facility cannot replicate. There are several models [17, 18] to predict the general compressibility effect on an axial compressor.

Nevertheless, even if general trends can be predicted with some confidence, it is hard to argue that the specifics of shock interaction with stall mechanics, end wall mixing and tip leakage can be predicted accurately using simple models [19]. Both Ref. [20] and Ref. [21] outline design methods applied to scale certain aspects such as blade loading when scaling a high-speed design to lower speeds, but neither has a detailed comparison between the two. The rationale from Ref. [22] can nevertheless be used to assess areas in which the impact from compressible effects are expected since they scale to the magnitude of Ma number. The relative Ma number in the rotor blades increases with radius, and for a typical high-speed LPC, the Ma number is below 1 for span locations below approximately 50%. Therefore, the most significant discrepancy between high-speed and low-speed cases is expected to be near the shroud.

2.2.5 Effects of rotor tip-clearance

Tip-clearance primarily affects the secondary flow structures near the shroud, either by leakage through the tip clearance or by the scraping of the low momentum boundary layer at the shroud [22]. A smaller tip clearance will reduce the leakage but increase the scraping of the boundary layer. Sakulkaew [23] showed that for transonic compressors, there should be a minimum theoretical loss between the competing loss mechanisms at a relative tip clearance height, ε/h, of $0.1\% - 1\%$ (channel height h). Below a clearance of 0.4%, [23] and [24] computed similar stage performance with and without tip-clearance. The tip-clearance effects on stall margin are often evaluated by the pitch-line gap g to tip clearance, where values below 0.01 do not affect the stall margin. To allow features caused by both leakage flow and scraping, a relative tip clearance (ε/h) of 1%, $\approx 0.75mm$ or $\varepsilon/g = 0.022$ is selected for the baseline compressor. The tip clearance can be varied locally by in-situ adjustment or for a whole stage by replacement of shroud inserts made of Ureol®. The relatively large tip clearance of $\varepsilon/h = 1\%$ reduces manufacturing costs on the rotors and the shroud, since a larger throw is acceptable. A sensitivity analysis using the correlations from [18] and [22] provide performance variations in the order of $0.5 - 1\%$ for a throw of $\pm 0.075\,mm$.

2.2.6 Engine similitude

With the compressor parameters set, the aerodynamic design of the compressor was iterated between the experimentalist and the aerodynamic designer. The aerodynamic designer generally strives to match the engine similitude with the reference engine, fundamentally limited by the power available. On the other hand, the experimentalist attempts to optimise measurement conditions and reduce manufacturing prices. As a result, the iterative process is rather challenging, with numerous conflicting design demands. An initial set of design iterations were performed at Chalmers using in-house tools. With a satisfactory design at Chalmers, a few final design iterations were performed at GKN Aerospace. The aerodynamic design, from zero-dimensional to three-dimensional numerical simulations, follows the practice detailed in [1]. The numerical simulations of the LPC are detailed in [25].

One of the most reoccurring discussions during the design process was the channel height, and it serves as a good example. A smaller channel height was preferred from an aerodynamic perspective. However, a reduced channel height leads to increased wind speed and rotational speed, increased blockage effects from probes, decreased spanwise probing resolution and decreased blade size, all of which increase manufacturing complexity or limit instrumental access.

The final LPC design at ADP compared to the engine similarities reference engine is shown in Figure 2-5. The variation from the reference compressor of the presented engine similitude is less than 5% for all factors except Reynolds number Re_c and Mach number.
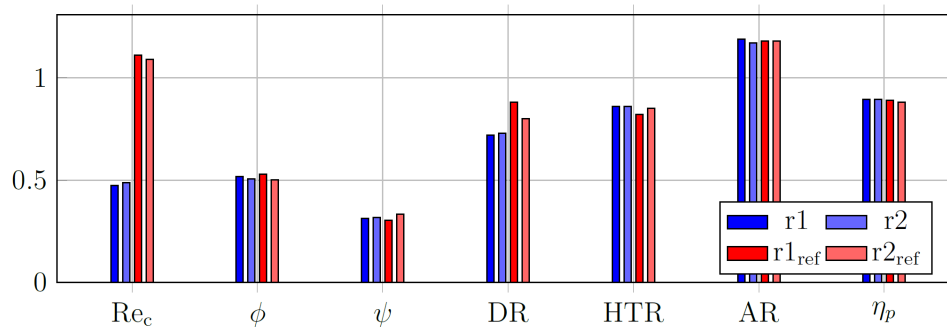
Figure 2-5 Facility compressor parameters in comparison to reference engine parameters. AR - Aspect ratio; HTR - Hub-to-tip ratio; DR - Degree of reaction; Re - Chord based Reynolds number; ϕ - Flow coefficient; ψ - Stage loading; η_p-- Polytropic efficiency.

2.2.7   Rotor mechanical design

The target of the mechanical design was to ensure the rotor's mechanical integrity. Since most of the simulations could not be verified before manufacturing, a conservative safety factor was targeted, and designs were selected that allowed for post-hoc failure mode mitigations. The summary given in the present section contains some aspects of the mechanical design of the low-pressure compressor unit.

The rotor assembly is designed with two independent discs for each rotor row and is mounted in an overhang configuration with most of the rotating mass extended outside two bearings. The two-disc configuration is not the mechanically optimal design, and it is seldom used in commercial engines, where a layout with rotors mounted on a drum, supported on each side, is often preferred. The concept implemented was a trade-off to maximise access and versatility of the facility. The large overhang mass was possible due to the vertical configuration of the facility, where loads from gravity are axisymmetrically distributed. The lack of a bearing downstream of the compressor allowed the OGV and ICD to be designed without consideration for mechanical load transfer, which greatly enhanced access and modularity. The two-disc configuration has lower hub leakage compared to a drum and was substantially more cost-effective.

A multitude of solutions to manufacturing the rotor blades were iterated, where the final candidate was an aluminium CNC blade with an isosceles trapezoid (UK definition) mount. This mount provided a reasonable balance between manufacturability, price and stress distribution.

The mechanical integrity of the rotor was ensured by first addressing the static loads and later transient loads. The rotor is exposed to periodic loads and necessitates structural simulations to assess fatigue failure. A maximum operational time of 5000 hours in 8-hour intervals was selected as this would cover the facility expected operation period. A gross overestimation of the dynamic load was selected by assuming that the blade would perceive the highest simulated load at each wake passage. With 124 stators at 1920 RPM for 5000 hours, this leads to a single rotor blade perceiving 7.2×10^9 cycles. The confidence of cycle fatigue load generally decreases with the number of cycles, primarily due to the dependency of environmental effects, the quality of the surface and any internal material impurity that might initialise the first crack.
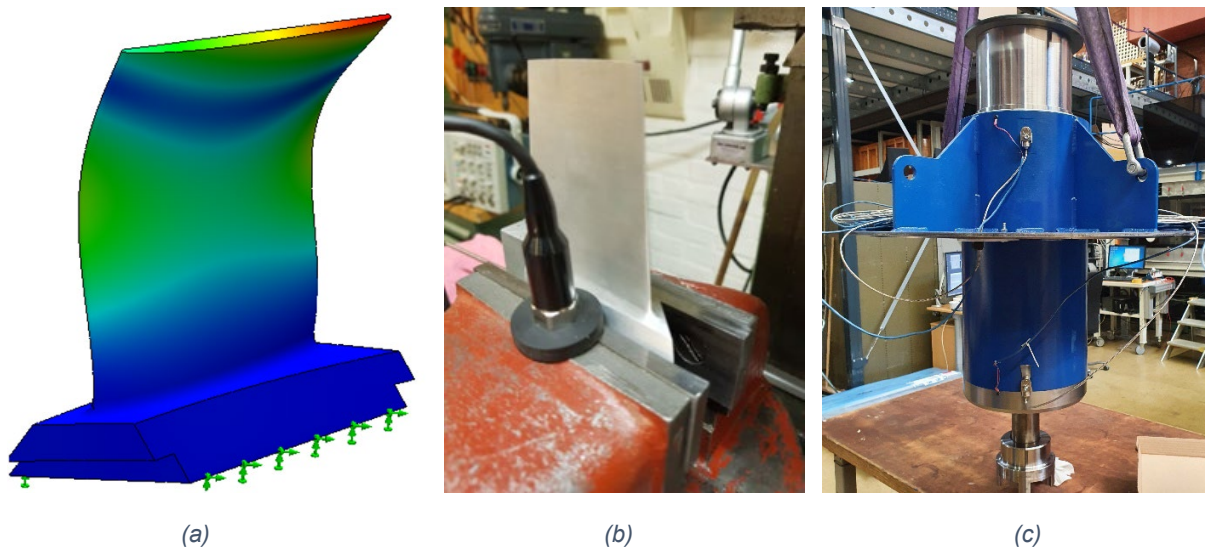
Figure 2-6: (a) Mode 3 of CooperV2 R1 simulation; (b) single blade ping test of the machined CooperV2 R1 geometry; and (c) the assembly with rotor housing before mounted in the facility.

The modal simulation of the two rotor blades impacted the aero design. Several complete redesigns were required to mitigate excitation modes near or precisely at the operational range. The modal simulation was verified by a ping test on manufactured samples together with the department of structural dynamics at Chalmers. The ping set-up is shown in Figure 2-6b where the blade is mounted only in the lower edges in the wise. The test matched the third mode at 2709 Hz shown in Figure 2-6a of a dynamic structural simulation within 1.2% difference. As a side note, the number of blades was changed from 60 in early versions to 61 (prime) to mitigate divisors near the excitation frequency.

A rotor housing was designed to allow for machining the bearing seats in one process (mitigates issues with bearing alignment). The housing contains all rotor monitoring instrumentation and allows for several steps of the shaft mounting to be performed outside of the facility. The rotor housing substantially simplified assembly is shown in Figure 2-6c.

2.2.8 Design of the intermediate compressor duct

This section describes the general design of the intermediate compressor duct. The baseline aero design was performed at GKN. The design of the ICD was targeted to be a more aggressive design in terms of radial reduction relative to the length of the duct, $\Delta R / L$. The aim was to stress critical parts of the duct without large-scale separation. An aggressive duct provides a reasonable starting point for design attempts to shorten the duct with a heat exchanger integration. Representative values of ICD design parameters such as inlet channel height to duct length h/L and inlet to outlet area ratio A_o/A_i were sought and guided the compressor's design.

2.2.9 Dimensioning

Table 2-1 shows fundamental design parameters and typical values for three different design domains, the selected baseline design and open access geometry of the VINK compressor presented in [1]. Fundamental design parameters are the relative radial variation to the duct length $\Delta R / L$, inlet channel height to duct length h_i/L, the outlet area relative to the inlet area A_o/A_i and the loss coefficient, which is the total pressure losses relative to the inlet dynamic pressure $Y_p = \left(P_t - P_{t,in}\right)/q_{ref}$ as defined in [26]. "Very aggressive" ducts are defined as ducts with large-scale hub separations and total pressure losses of $Y_p \geq 0.1$. Ducts with small or limited separations and losses in the order of $Y_p \approx 0.1 - 0.05$ are defined as "aggressive". "Conventional" ducts are defined where little or no flow separation occurs leading to losses in the order of $Y_p \leq 0.05$. Note that the ranges of the three design domains, "very aggressive", "aggressive" and "conventional", are arbitrarily derived from figures, results and tables in [26, 27, 28] by the authors. The study of Ortiz Duenas [26] was largely used to categorise the duct designs based on pressure loss coefficient Y_p. Duenas studied a representative modern S-duct with a $\Delta R / L = 0.5$ where no separations were visible. A re-optimised duct with $\Delta R / L = 0.67$ increased losses slightly while an optimised duct with $\Delta R / L = 0.78$ had a rapid increase in losses due to large-scale hub separation.

Table 2-1: Table of ICD design ranges from very aggressive to conventional together with selected baseline design for the ICD and the open geometry of the VINK compressor.

	Very Aggressive	Aggressive	Conv. [26]	Baseline	VINK
$\Delta R\,/\,L$	$0.6 - 0.9$	0.6	0.5	0.64	0.41
$h\,/\,L$	$0.15 - 1.3\,*$	$0.15 - 0.3\,*$	$0.15 - 0.3\,*$	0.43	0.6
A_o/A_i	$0.8 - 1\,*$	$0.9 - 1.15\,*$	1	0.99	1.15
Y_p	≥ 0.1	$\approx 0.1 - 0.05$	$\leq 0.01 - 0.05$	0.06	$-$

*Estimated from figures in publications [27, 26, 28, 29].

Throughout the facility design, a relative high channel height was sought due to the many benefits such a configuration brings to most probing instrumentation. Due to geometrical constraints, several feasible configurations within the LPC design space were not possible within the ICD design space. The limitation can be derived from the targeted area ratio of $A_o/A_i = 1$, the targeted LPC radius $R_{1,mid}$ together with a high ratio of duct turning to inlet midspan radius $\Delta R/R_{1,mid}$. Combinations occurred where the geometrical hub radius at the outlet was below zero.

From the definition in Table 2-1, one may note that the baseline design can be categorized in the "aggressive" to "very aggressive" domains with losses in the order of $0.05 \leq Y_p \leq 0.1$.

2.2.10 Design and aerodynamic simulations

With the selected feasible design target, the final aerodynamic design was provided by GKN and simulated at Charmers as part of the LPC simulation using Ansys™ CFX 2019 R1 with the turbulence model $k - \omega$ SST, mixing plane and enhanced wall functions. Details of the numerical simulation are presented in [25].

2.2.11 Construction of the ICD

The versatility and access of the ICD was considered crucial since more design iterations of the ICD are expected compared to other components such as the OGV or the LPC. A few design choices were essential to achieve a versatile ICD module. The vertical design and the upstream flow restrictor allow the ICD to be placed with an open-ended outlet, this permits access from all directions for both instrumentation and personnel. To further mitigate design limitations inflicted from other subsystems, the ICD module is separated from the traverses, instrumentation and other structures such as the OGVs. Separating the modules allows the ICD to be rapidly replaced with minimal effort since the aero surfaces in the ICD only interferes with the facility by a small amount of contact surfaces and a few bolts. Furthermore, the OGVs, hub, shroud and struts in the ICD module can be individually replaced.

The final design of the baseline configuration of the ICD mounted in the facility is shown in Figure 2-7, containing colour-coded components that represent the different access types and locations. Red indicates the traverse system for ICD volume access, blue for the LPC outlet's traverse access, yellow for traverse and optical access within the LPC, and the green represents radial access within the LPC. Key components are marked in Figure 2-7 such as rotor blades and stator vanes, probe access and other instrumentation, some of which are described below. Figure 2-7 shows the measurement boundaries B_A to B_C; these are described later in this report together with the rationale for instrumentation.
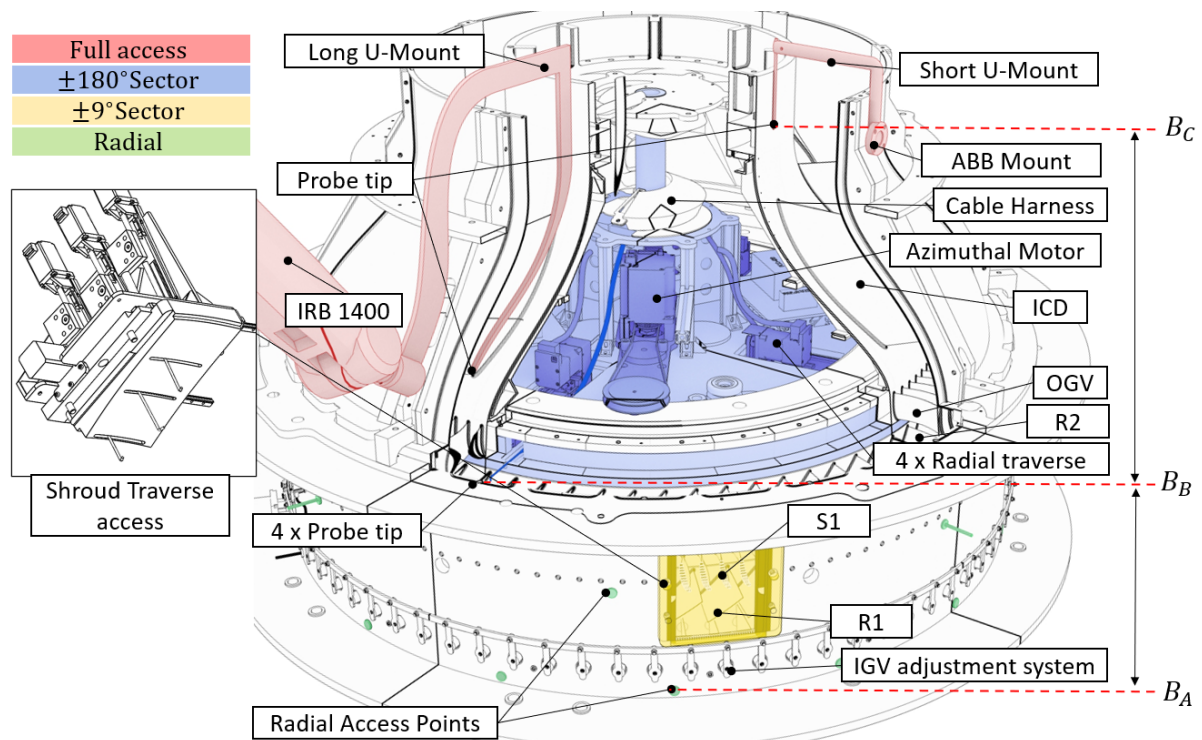
Figure 2-7: Schematic illustration of the baseline ICD instrumentation, traverses mounted on the LPC unit. See text for further information.

More than fulfilling the aerodynamic purpose of the OGV, the OGV module provides mechanical support through the gas path for the hub-mounted traverse module and ICD. The OGVs can also be instrumented or substituted, either as individual vanes or as one of the 14 modules of nine OGVs.

A hub-mounted traverse system was selected as it allows for easy 360-degree access upstream of the OGV without penetrating the LPC containment. The already present axial gap between the LPC and the OGV allows for relatively relaxed manufacturing tolerances, and the interface could be machined relatively cost-effectively. A similar hub-mounted traverse downstream of the OGV was neglected as in this access location any protrusion at the hub downstream of the OGVs could potentially have a significant effect on the turning ability of the duct.

Several designs of traverse access through the ICD shroud were attempted for the outlet and intermediate planes in the ICD. However, a robotic arm was found to be the more cost-effective and versatile traversing equipment to access the ICD domain, as little to no modification would be required between each ICD iteration. Shroud mounted traverses are expected to be used in some ICD configurations but will be part of the ICD specific instrumentation and assembled outside the facility.

2.2.12 Traverse details

The final design uses an ABB RBK-1400 robotic arm as shown in Figure 2-7. The positional accuracy of a robotic arm is inversely proportional to the distance to the mounting point, and the distance from the downstream facility outlet to the OGV outlet is around 400mm. No robot on the market was identified that could position the probe tip within suitable tolerances if the probe tip distance to the mounting point was 400mm. A U-probe has been designed, which mitigates the need to penetrate the shroud and still have low position uncertainty in the probe location. This configuration is suitable for low-speed applications where probe blockage has a limited upstream effect, and forces on the probe holder are relatively low. The hub-mounted traverse system includes four radial traverses based on Nanotec PD2-C4118L1804-E-01 and Misumi LX2001P-MX-B1-F-200. Each traverse system shares the same mounting point and can move individually. The whole traverse assembly rotates tangentially where the load transfer to rotate the traverse system is accomplished by an inverse T3 timing belt set-up. The timing belt is glued inside the HepcoMotion R-76-799-r360 ring, and a T3 timing pulley is mounted on the rotating traverse. A Nanotec PD6-C8918S6404-E-09 with a gear ratio of $31:1$ by two belt reductions provides the motion control to the T3 timing. The internal diameter of the HepcoMotion ring is not divisible by an even number of T3 teeth, and the missing pulley was replaced with a mechanical stop. Therefore, the traverse system cannot provide true 360-degrees access for an individual probe since it

is missing roughly $0.5°$. There are four individual traverses, so 360-degree access is still true for the system. The $31:1$ gear ratio between the motor and the T3 pulley was required to provide sufficiently high tangential resolution. Furthermore, the large Nanotec PD6 stepper motor was selected to handle aerodynamic loads on the traverse system from the second LPC rotor and the four probes inserted into the highly swirling LPC outlet air. The traverse system is fully exposed to the LPC rotor with only $1 - 5mm$ axial distance. The mechanical stop inside the HepcoMotion R-76-799-r360 ring hinders free rotation of the traverse system if braking power of the Nanotec PD6 motor is lost.

2.3 Instrumentation

The instrumentation was central throughout the iterative design of the facility. Design choices were ultimately evaluated from an instrumentation perspective by assessing the expected measurement quality with various levels of fidelity, from simple MCS of the subsystem to an extensive pre-test evaluation as presented in [25]. The instrumentation and control systems were organized in a hierarchy of modules with mapped out evaluation chains, which provides an overview of the instrumentation and is shown in Figure 2-8.

The information flow is illustrated as solid arrows where the thick arrows represent network communication between the modules. Subsystems within each module are marked with white background and italic text, such as the ABB ACS250-800 motor controller, shown as ABB or the inlet mass-flow controller shown as $\dot{m}$ in the schematics. The boxes with the white background and dotted border are input variables used to calculate sought quantities. One can notice redundancies of measured quantities for one sought quantity, for example, the load coefficient ϕ. For monitoring, the load coefficient is derived from mass flow and shaft input power. This is suitable for monitoring purposes due to the direct sampling time, but it is unsuitable for performance evaluation at this facility, as shown in [25]. For performance evaluation, the same coefficient is calculated from gas-path studies in the traverse module. The same is true for pressure ratio, which is calculated using static probes for monitoring but by gas-path studies for the performance evaluation. The flowchart also shows some of the measurement pathways; RPM can be derived from both the ABB motor controller and the rotational trigger on the shaft.

The central part of the facility is the control unit, which ensures the facility's safe operation. Other modules are added to expand the instrumentation. The monitoring module is running on a PC using LabView™ and a RealTime module NI-9504. The build-in FPGA in the NI-9504 performs low-level analysis on accelerometer and high-speed voltage signals such as rotor encoder and tip-clearance monitoring. The NI-9504 digital and analogue interfaces are expanded using the National instruments REM series. These REM modules have a relatively slow update rate and are therefore only suitable for monitoring and control of $\dot{m}$ and cooling system logic. The traversing module with internal modules for data acquisition such as multi-hole probe set-up or hot-wire anemometry as described in [30], [31] and [3]. Another separated module is PIV and heat transfer and laminar-turbulent transition investigation by IR-thermography. The IR-thermography method is described in [15] and [3]. The individual modules communicate to the facility primary over a local network, digital port for low-level communication and TTL signals for more time-sensitive triggers.
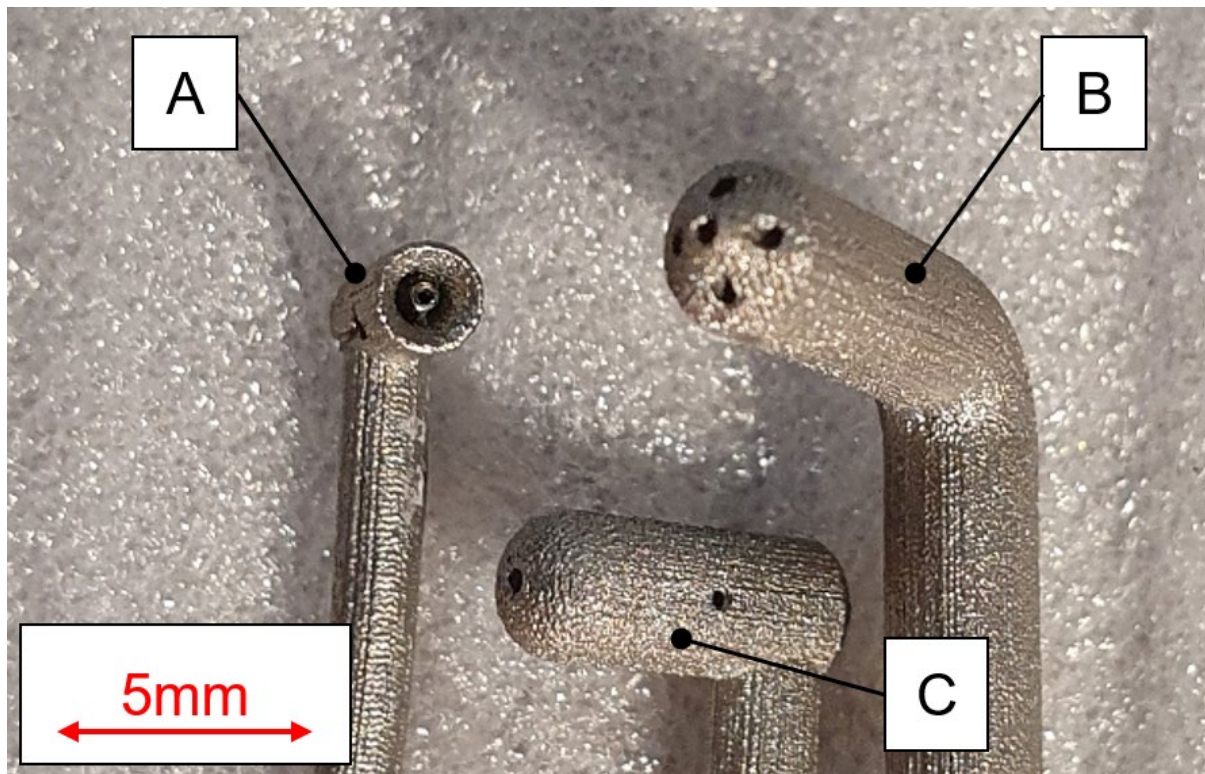
Figure 2-8: Flowchart of signals, data processing and sampling devices for different modules in the facility.

2.3.1 Pneumatic Measurements

The pneumatic instrumentation in the LPC and ICD is comprised of both single and multi-hole probes. of different sizes and manufacturing methods. The pneumatic probes in the LPC-ICD test facility are manufactured using high precision binder jetting by DigitalMetal® AB and calibrated in the Chalmers in-house calibrator. A 1.8mm diameter Kiel probe, a 2.8mm diameter Prandtl probe and 5HP manufactured by DigitalMetal® AB are shown in Figure 2-9.

Figure 2-9: Pneumatic probes for baseline instrumentation inside the LPC and ICD manufactured by DigitalMetal® AB, (A - Kiel probe, B - 5HP, C - Prandtl probe).

Details about the uncertainty assessment of the pneumatic probe measurement in the LPC are provided in [3]. To clarify the experimental set-up, Figure 2-10 shows the general outline of the information flow in the LPC and ICD with details of the pneumatic and temperature measurement devices. Figure 2-10 illustrates the core unit with access location and the configuration of investigating boundary B_A, B_B and B_C by probing and pressure taps on the strut. Following the flow direction, the first pneumatic measurements are in the contraction, where an FCO-432 measures the differential static pressure over the contraction. The solid black line illustrates the positive reading port, and red represents the negative and is henceforth referred to as the reference port. The grey boxes outlined with solid black lines are solid-fluid interfaces where the pressure is measured. Each interface requires detailed consideration but is ignored on a system-level. The FCO-432 provides a cost-effective and stable single-channel measurement and is easily calibrated against the FCO-560 micro manometer. Downstream of the contraction, Kiel and Prandtl probes are inserted into the flow. All Kiel probes in the LPC and ICD are identical with an outer diameter of 1.8mm. The inlet Kiel probe is differentially connected by the FCO-560 to the statically mounted Kiel probe at boundary B_B. There are two Kiel probes at boundary B_B, one used for total pressure normalisation and one for pressure rise (Π) measurement in the LPC. The inlet is accessed by inserting a probe radially through the shroud via 10mm diameter holes. Radial inlet total pressure, velocity and static pressure profiles are gathered by radially traversing a Prantl probe through the 10mm hole. The Prantl probe is differentially connected to another Prandtl probe permanently mounted at boundary A at another tangential position for normalisation. The measurement is repeated at several azimuthal locations around boundary A to provide the variations along the inlet. All pneumatic pressure measurements in the LPC and ICD are gatherer by two ESP-32HD units referenced to the statically mounted Kiel probe at boundary B_B. Pressure measurements inside the LPC, such as static blade pressure or pneumatic probes mounted on the 18° traverse system, utilise an ESP-32HD with piping through the shroud. A second ESP-32HD, located inside the ICD, is used for all the pneumatic measurements in the gas path of the ICD with the Run Ref connected to the same statically mounted Kiel probe at B_B. The pressure tap implementation on the strut and shroud is near identical to another facility at Chalmers, with pressure taps printed in SLA vanes and hubs as described in [32].

2.3.2   Temperature and heat transfer measurements

Figure 2-10 includes the basic set-up for the temperature measurements in the LPC and ICD following the same schematic indication as in Figure 2-8. Following the flow direction, the temperature is measured at the inlet boundary B_A using three PT-100 delivered from Pentronic. The PT-100 is shielded

in an SLA manufactured mount to mitigate shunt offset and static temperature offset. Identical probes are used for all stagnation temperature measurements. At B_B and B_C one sensor is permanently mounted while the other is mounted on the traverse system. The PT-100 probes between interface B_A and B_B are used to evaluate LPC baseline performance during ICD studies. The Pentronic PT-100 RTD elements are accredited down to uncertainty of 0.02K. The NI-9127 used to sample the RTD temperatures in the LPC and ICD can provide this resolution but with a device bias offset of ± 0.1K.
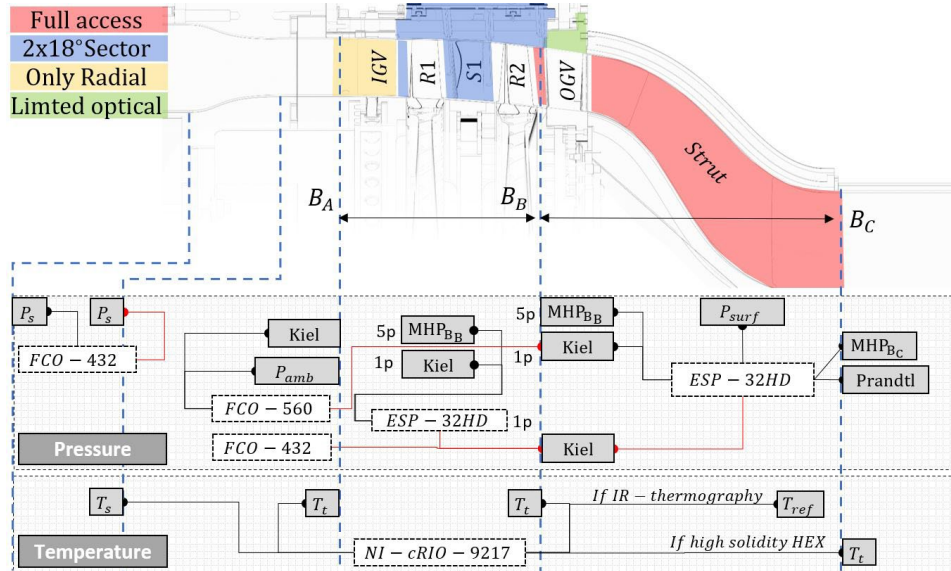
Figure 2-10: Flowchart of signals and instrumentation location in the LPC and ICD.

In Ref. [15] the implementation of IR-thermography to measure the convective heat transfer coefficient and detect the laminar-turbulent transition is described. The ICD is designed to accommodate the same method on strut, hub and shroud. Optical access is granted to the hub and most of the strut without penetrating the hub or shroud line. Reflectors, mirrors or drilled holes will provide optical access to the leading edge and potentially to the shroud. A schematic of an instrumented hub segment manufactured by additive manufacturing is illustrated in Figure 2-11. The water is pumped into the lower collector box, pushed out into the channel, and collected in the outlet collector before exiting the test section. Using this set-up hinders high-quality heat transfer measurement near the very start and end of the ICD hub line. The current setup hinders high-quality heat transfer measurement near the start and end of the ICD hub line due to high uncertainty in the inner wall heat transfer rate. However, the area is heated, so transition or separation will be possible to detect.
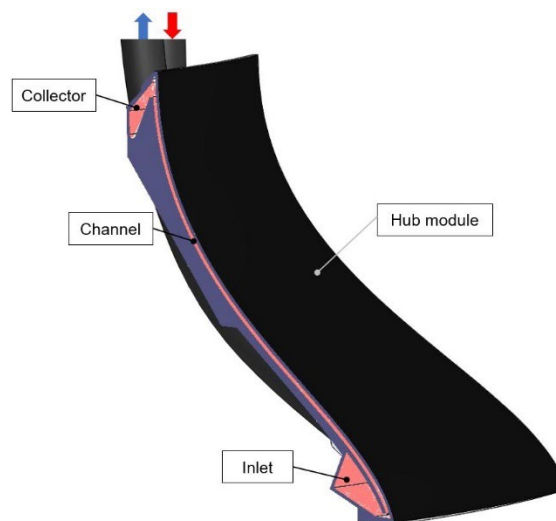

Figure 2-11: Hub segment for heat transfer measurements in the ICD with water entering at the inlet and exiting at the collector. The black surface is in contact with the core flow in the ICD.

2.4 Pre-test Evaluation of Low-Pressure Compressor

Before final manufacturing, the instrumentation in the LPC was evaluated by a pre-study using the numerical results from the existing CFD model (i.e. the model used during design). The pre-study was undertaken by virtually performing all the expected steps during an experimental test campaign to find issues and devise potential mitigations before the final design was commissioned for manufacturing. This section provides a general description of the detailed pre-study. Detailed information can be found in Ref. [3].

The target was to measure these with a maximum error of 1% and Ref. [3] describes the processes to achieve this. Measuring mass flow with an accuracy of 1% in a large-scale facility is challenging. However, mass-flow measurements can be performed outside the compressor unit, and future work could be dedicated to address this issue. Furthermore, to avoid errors from mass flow measurement propagating into other compressor performance parameters, these need to be isolated from the mass flow. In doing so, efficiency cannot be measured by any means such as shaft power[1] or thermal balance of the system, as these require mass flow as a variable input. Since the instrumentation to measure flow properties by traversing was already required for flow field investigations, the idea is to utilise these further to calculate the performance of the compressor. The foremost challenge in measuring the performance of an $80 - 91\%$ efficient LPC is the low temperature difference between the inlet and outlet of the compressor. To accurately capture this temperature difference, great care is needed.

Performing a pre-test evaluation on the numerical flow field, instead of the experimental flow field, is beneficial since design changes in the digital twin geometry are practically free when compared to modifying already manufactured components. There are some limitations when using the numerical flow field; the flow field is modelled and will, for many reasons, not perfectly reflect the final experimental flow field. However, there are somewhat less apparent benefits of using numerical results for these kinds of studies where the predominant ones are the controlled environment and simple integration of the flow field. The controlled and stable environment allows for features to be evaluated individually, something that might be impossible or very time consuming to perform experimentally. For example, in [3] the required traverse mesh density is determined to capture the average flow values within a targeted accuracy. Numerically it is relatively simple to interpolate a boundary with variable mesh density until a satisfactory difference to boundary average is achieved. If the numerical flow field is representative, the study provide critical information and specification to the instrumentation such as resolution and maximum allowed probe size. The same mesh study is required to be performed with experimental data but these are available at the design stage and will be influenced by operational fluctuations, measurement errors and instrumentation limitations. From the pre-study performed on the LPC, dominant error sources could be divided into four groups, single-point accuracy, normalization error, data normalization and error propagation. A brief description of these is given below:

Single point accuracy is the measurement error at a given point. The probe does not read the actual value, and the probe itself interferes with the flow field. In short, the transducer error was addressed by acquiring the best transducers on the market and minimising the reading range to the absolute smallest allowed, which in this case, is different between the inlet and outlet. A probe might be mis-reading the value in the flow as too high gradients over the probe area or other interference with the probing port. The ratio of a probe reading and real fluid properties is often referred to as the recovery factor. One way to mitigate the effect from the recovery factors when performing differential measurements is to use identical probes in similar flow fields since the offset is similar at both locations. The axial location of the compressor outlet evaluation plane was adjusted to maximise similarity to the inlet plane sole due to this. The influence of the probe on the flow field was not investigated. The relatively low-speed nature of the facility and small probes leads the author to expect minimal effects from blockage on the reading on the probe but was not further investigated.

Traverse discretisation error is the difference between the actual mean flow properties and a discrete sampling of the flow. By interactively increasing the mesh density, a sufficient cover ratio is identified. As a note from the pre-study in Ref. [3], it is highlighted that it is improbable that rakes of $8 - 10$ points as recommended in PTC 19.5 are insufficient to gather gas properties within 1% error in most applications.

---

[1] Shaft power further introduces a number of challenges with bearing and viscous losses not related to compressor performance.

Data Normalisation is briefly presented in Ref. [3] For this report, each measurement is presented as normalised with the interface average. Normalised total pressure is presented as the fluctuation of total pressure over the mean of the interface

Error Propagation with single point measurement and discretisation uncertainties estimated, the final error, including data normalisation, is estimated using error propagations as described in Ref. [3].

The final uncertainty for test configurations optimised for measuring the isentropic efficiency of the compressor is shown in Figure 2-12, where Π is the stage loading, $\dot{m}$ the mass flow and η_{is} the isentropic efficiency. On the vertical axis, the errors are given as a percentage, and the different colours indicate the contribution for the different error source and the total estimated error source. The total pressure ratio can mainly be limited by the FCO-560 accuracy and discretisation (blue) and normalisation (orange) have little effect. As mentioned before, it is challenging to achieve mass flow measurement uncertainty below 1% due to the discharge coefficient. Uncertainties of isentropic efficiency below 0.5% are shown in Ref. [3] and Figure 2-12, where the main contributor is the differential temperature measurements.
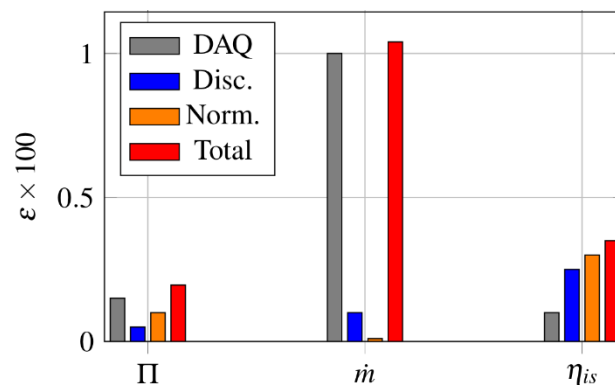
Figure 2-12 - The bar diagram showing estimated uncertainties of the stage loading, mass flow $\dot{m}$ and isentropic efficiency η_{is} with the total uncertainty shown as red, discretisation as blue, normalisation as orange and single point acquisition as grey

The authors would like to comment that even though the study in Ref. [3] shows promising results and provides insights arguably impossible to achieve with experimental studies, the uncertainty analysis was performed on numerical data. Thus, error sources are certainly overlooked, and unknown issues are to be expected when experimentally implemented. However, with an error estimation indicating a less than 0.5% uncertainty, it is arguably likely that an error below 1% should be achievable but would require a separate experimental effort due to its arduous nature.

3 Approach for heat management verification

Numerous subsystems of the facility were evaluated and commissioned during its development. For example, all the pneumatic probes used in the LPC and ICD were designed in-house and evaluated at Chalmers Fluid and Thermal Sciences laboratory probe calibrator before being mounted in the facility. Moreover, the compressor performance was evaluated with a simplified ICD duct during the commission and the accelerometers for rotor vibration were tested during mounting. The results from the commissioning of these subsystems are separate from this report, and this report focuses on the facility's key performance aspect that contributed to the modelling of core heat management modules. One of the primary targets for the facility was to accommodate investigation and verification for models in the OGV-ICD domain. Before detailed studies of the OGV-ICD domain are performed, the operational stability of the facility was assessed. The OGV-LPC inlet measurement is a few mm from the trailing edge of the second rotor of the LPC. The LCP operational pressure ratio is approximately 100 times the expected average total pressure drop we seek to investigate between the OGV inlet and the ICD Outlet. As described earlier in this report, there are several challenges with a detailed investigation of a low-loss unit, such as the OGV-ICD, just downstream of a high-power unit, such as an LPC. Miniscule variations in the LPC's operation are likely larger than the entire total pressure drop over the ICD. Even though data reduction for the OGV-ICD domain is performed, the operational stability is of interest. The first step in assessing the facility's suitability to conduct studies in the OGV-ICD domain was to assess the operational stability and effects of any variation on the selected methods on the data reduction. Furthermore, the facility is built to access 360 degrees of the OGV-ICD domain with five different probes (four at the OGV inlet and one at the ICD outlet). The annular access provides an excellent possibility to assess the tangential uniformity of the compressor. A rotor outlet uniformity study further assesses any potential effect from upstream instrumentation and if any local considerations are required. The overall uniformity of the domain is assessed by traversing the midspan for a 340-degree sector. A single line at midspan was selected due to the high trade-off between sample time and the utility of the gathered data. A study of the full compressor with the resolution used to resolve OGV wakes would require 55,000 samples which take around 2.6 days to sample. A single line for a 340-degree sector has a sample time of 1 hour and provides sufficient information to assess tangential variations of the boundary. The inlet and outlet of the OGV-ICD are later investigated with increasing resolution until sufficient mesh resolution is found. The required data for numerical verification is primarily comprised of radial profiles at the inlet, plane outlet measurements and heating capabilities of surfaces inside the duct. A photo of the facility after completion of the experimental test campaign is shown in Figure 3-1. An inspection hatch is opened on the shroud in the ICD to visualize the internal instrumentation. The IR-camera is mounted as well for gathering heat transfer experimental data, shown later in this report. The facility can be operated remotely, outside the laboratory, but as can be seen in Figure 3-1, it is highly accessible for ICD studies.

Figure 3-1 The upper floor of the new compressor facility after the completion of the experimental test campaign. The probe calibrator can be seen to the left and the IR camera mounted at the ICD outlet.

By the end of the test campaign, 25 operational points were successfully investigated in detail. The arguably most challenging operational point is the rotor at half speed, N0.5, since the instrument readings are the lowest and have the highest ratio of instrument noise to reading. The lowest pressure

ratio is found at N0.5 and the stability of the motor and system can be evaluated in detail. All relevant aerothermal data used for validation of the numerical models have been normalised with a reference at the axial position, or for the selected operational point to better illustrate features in the dataset. In the result section a selected case of the dataset is presented to illustrate the aerothermal effects of an LPC running off-design on the OGV-LPC.

4   Numerical model and methods for heat transfer simulations

The final design of the low-pressure compressor in the facility was performed numerically and is presented in [3] and [25]. This section is based on the same geometry and similar numerical set-up where ANSYS TurboGrid was used to generate structured, hexahedral meshes of the LPC. The first node height of the mesh was set below $y^+ = 1$. The solver ANSYS CFX 2021r1 was used for simulating the flow field, solving the compressible flow equations (RANS) together with the $k - \omega$ SST turbulence model and using the gamma-theta model to simulate laminar-to-turbulent transition. The working fluid was set either as an air ideal gas or as a semi-perfect gas with temperature dependent properties. The compressor properties, design point operational conditions, and geometry for the baseline simulations are shown in Figure 4-1.

ENABLEH2 Compressor	
Rotational Speed	1920 rpm
Mass flow	17 kg/s
Pressure ratio	1.07
Tip Speed	100 m/s
Axial Velocity	70 m/s
Rotor Re_c	600 000
Avg Tip radius	620 mm
Avg Hub radius	540 mm
N. stator Blades (IGV, S1, OGV, ICD)	75, 126, 124, 8
N. rotor Blades (R1, R2)	61, 69
Avg Aspect Ratio	2.157
Avg Tip Clearance	0.75 mm
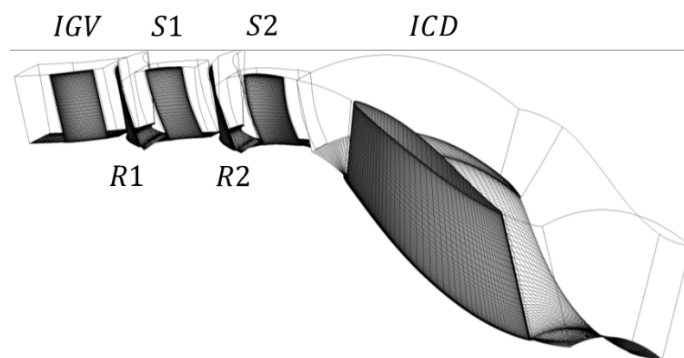
*Figure 4-1 **Left**: ENABLEH2 compressor properties and design operating point. **Right:** ENABLEH2 compressor geometry. The geometry is composed of an Inlet Guide Vane (IGV), Rotor 1 (R1), Stator 1 (S1), Rotor 2 (R2), Stator 2 (S2), and Intermediate Compressor Duct (ICD)*

4.1   ICD Refinement and verification

The ICD is the main target of the heat management system. However, numerical heat transfer studies require a higher fidelity compared to an overall performance evaluation, so a refinement was required. A case was created where the ICD domain was isolated from the baseline simulation to accommodate conditions required for heat transfer studies. The inlet to the ICD domain was derived from the complete compressor simulation by inlet radial profiles which were experimentally verified. At the outlet a static pressure of 1 bar was specified, which resulted in matching the design point mass flow. The hub and shroud were set as no-slip adiabatic surfaces, while the vane was set as no-slip but used two different types of thermal boundary conditions.

To accommodate for the effect of temperature changes in the boundary layer, the working fluid in the refined case was set as a semi-perfect gas with temperature dependent thermal conductivity and viscosity. This was implemented by curve-fitting 8th degree polynomials on data obtained from REFPROP [33] and implementing these as functions in ANSYS CFX. Transition was modelled by both the one-equation Intermittency model and the two-equation gamma-theta model [34], [35], [36]. The aero surface inside the OGV and ICD were set as hydraulically smooth.
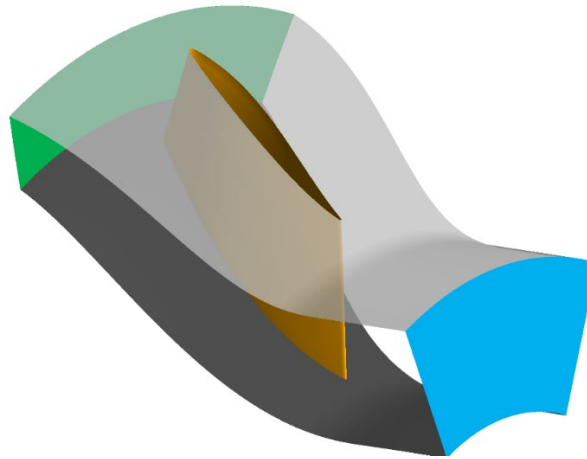
Figure 4-2 Domain setup: Vane surface (orange), hub (dark grey), shroud (light grey), inlet (green), and outlet (blue). Periodic surfaces not explicitly shown.

Instead of using constant temperature or heat flux for the thermal boundary on the surface, the initial thermal boundary was obtained from [15] and represents the heat transfer setup used in the outlet guide vane (OGV) of the existing Chalmers OGV-LPT test facility. A similar implementation of the same boundary conditions can be seen in Figure 2-11: Hub segment for heat transfer measurements in the ICD with water entering at the inlet and exiting at the collector. The black surface is in contact with the core flow in the ICD. for the hub in the ICD. This boundary condition assumes heat transfer through the vane is accomplished by flowing water through internal channels below the vane surface and that the heat transfer can be approximated as one-dimensional. In this case the heat transfer can be treated as a thermal circuit and its thermal resistance (per unit area) can be calculated as follows:

$$R''_{tot} = \frac{1}{h_{conv,air}} + \frac{t}{k} + \frac{1}{h_{conv,water}}$$

4-1

The initial approximation is that the thickness t of the wall between the channel and vane surface is 4 mm and the thermal conductivity of the vane is 0.2175 [W/mK]. The convective heat transfer of the water side is set to 3700 [W/m²K] [15]. In CFX the thermal resistance for the heat transfer occurring inside the vane itself can be used as a boundary condition in terms of an overall heat transfer coefficient U in an equation analogous to Newton's law of cooling (Eq. 4-2). The water temperature is assumed to be constant along the channel length due to high flow rate.

$$q''_x = U\big(T_{wall,air} - T_{\infty,water}\big)$$

$$U = 1/R''_{tot} = 53.59 \ [W/m^2K]$$

$$T_{\infty,water} = 305.15 \ [K]$$

4-2

5   Experimental Results

Results are presented at different measurement planes of increasing axial position, starting from the OGV inlet. The selected case is the "2022_08_02_N05_PR102_KiMhpHWT_IrBl_Mhp" which is approximately the operational conditions along the N05 speed line, representing the condition of half the compressor speed from the ADP, hence N05 ADP. Throughout the results section the selected case is referred to as N05 ADP. Finally, four more cases are shown to illustrate Reynolds number effects and off-design conditions. These cases are presented with respect to deviations from the N05 ADP case. One case is run at a higher speed line (N0.75) and with every other operation condition scaled along the rotational speed of the rotor. A final case is assessed along the speed line N0.5, where the pressure ratio is increased by 25%. Note that the pressure ratio specified in the file name is a control value and is not directly correlated to the pressure ratio of the facility.

5.1   Operational Stability

Figure 5-1 show the normalised monitoring parameters for the compressor at the selected case. The case consists of 2056 sample points and took just under 3 hours to sample. Variation in terms of corrected mass flow is shown as a blue line and varies with ±0.02 %. The variation in corrected mass flow is primarily cause by changes in ambient temperature and pressure. The variation on pressure ratio and RPM, shown as a yellow and a red line respectively, are negligible. For all the 25 cases the RPM varied with a maximum of 0.2 RPM during steady operation.
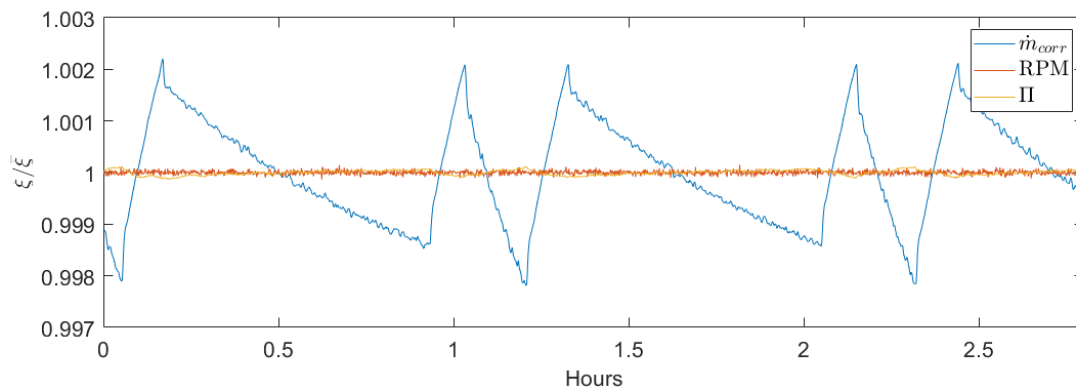
Figure 5-1 Operational stability in terms of corrected mass flow, RPM and pressure ratio of the facility running at N0.5 ADP.

The total pressure at the leading edge of an instrumented OGV over time is shown in Figure 5-2 with the total pressure reading divided by the assembly average shown in blue and normalised total pressure in red. Even though the operational variation of the LPC is miniscule as shown in Figure 5-1 the effect on the total pressure reading inside the ICD is substantial with variations up to 1%. For the normalised pressure the variations are in the order of 0.2-0.3 % which is the lower range of the uncertainty of the measurement.
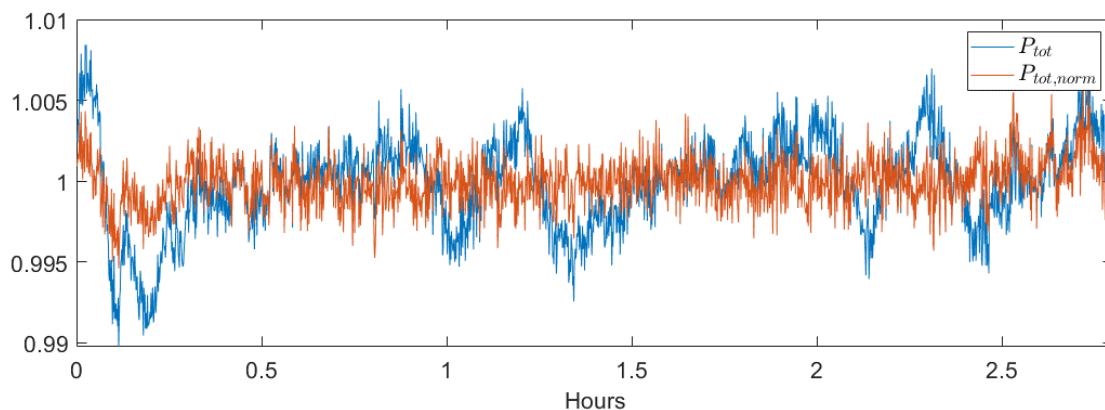

Figure 5-2 Total pressure readings of a Kiel probe mounted in the leading edge of an instrumented OGV together with the normalised total pressure for the duration of the reference case (N0.5 ADP).

5.2 LPC outlet Uniformity Assessment

Figure 5-3 shows total pressure and Figure 5-4 velocity magnitude along midspan in 0-340 degree sweep with steps of 0.5 degrees at the outlet of the second rotor. The total pressure was sampled with a Kiel probe and is illustrated with a blue solid line and the velocity magnitude with a 3mm MHP. Two solid black horizontal lines are used to illustrate variations of 1% from the sample average. One may note that most of the total pressure variations are around one percent with one clear peak at 180 degrees. Note that the tangential position of the Kiel probe has been offset 180 degrees so that this peak occurs at the same relative angle in Figure 5-3. The total pressure peak is accompanied by a drop in velocity of 1%. There are several potential reasons that could explain this local variation, all of which would require further investigation. However, the location matches well with a relatively thick upstream temperature sensor. The deviation above 1% is highly isolated, so the simplest mitigation path was to avoid detailed studies between 150 to 200 degrees and deferred the issues for later studies. Note that locally no time dependent normalisation was performed, hence Figure 5-3 shows instantaneous tangential variations of 1% magnitude. It is noted that larger deviations are common in many facilities.
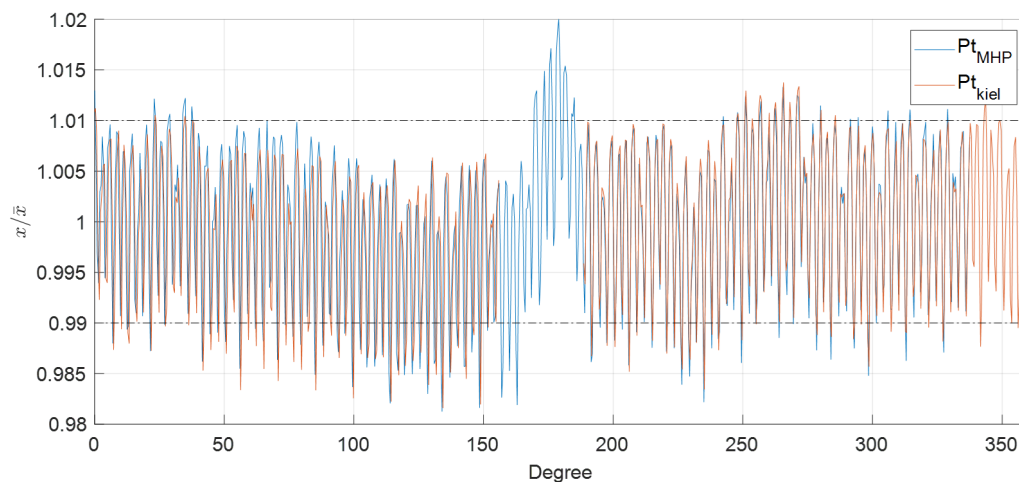
Figure 5-3 Total pressure variation at the outlet of the second rotor at midspan measured both by a MHP and a Kiel probe during the same experimental test case.
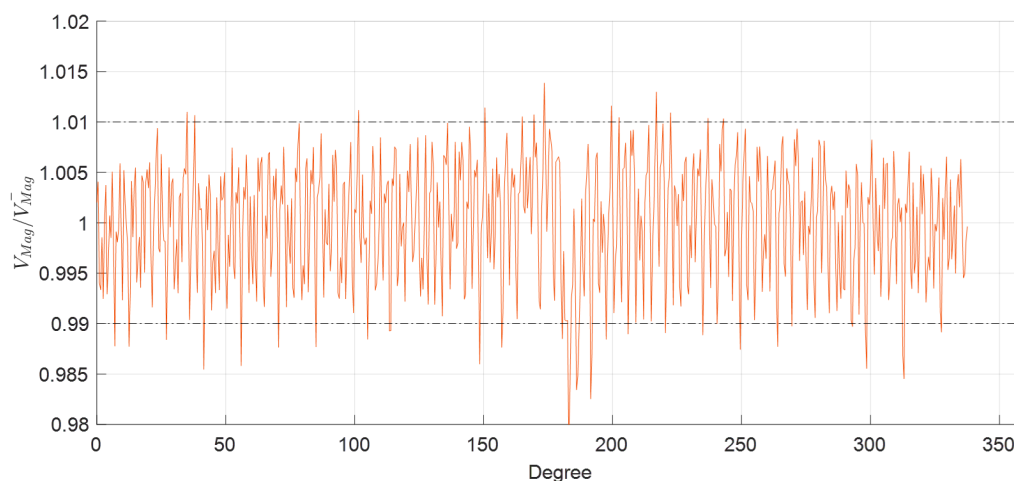

Figure 5-4 Velocity magnitude variation at the outlet of the second rotor at midspan measured by an MHP.

5.3 OGV inlet plane measurement

The LPC-outlet was studied over a 45-degree sector of 2065 points to match one sector of the ICD. The 45-degree sector is divided into three different tangential resolutions with identical radial resolution. Boundary layers are resolved with 10 points near the end-wall and with 15 radial positions uniformly distributed between the end-wall measurements. The probe diameter varies between each probe and hence the radial probe position is not the exact same position for each traverse. Tangentially the 45-

degree sector is investigated for 59 rows; 16 with a spacing of 2°, 22 with a spacing of 0.5° and 21 with the spacing of 0.2°. The mesh resolution is shown in Figure 5-5. The high-resolution study is focused on the centre and the low resolution in the outer domain.
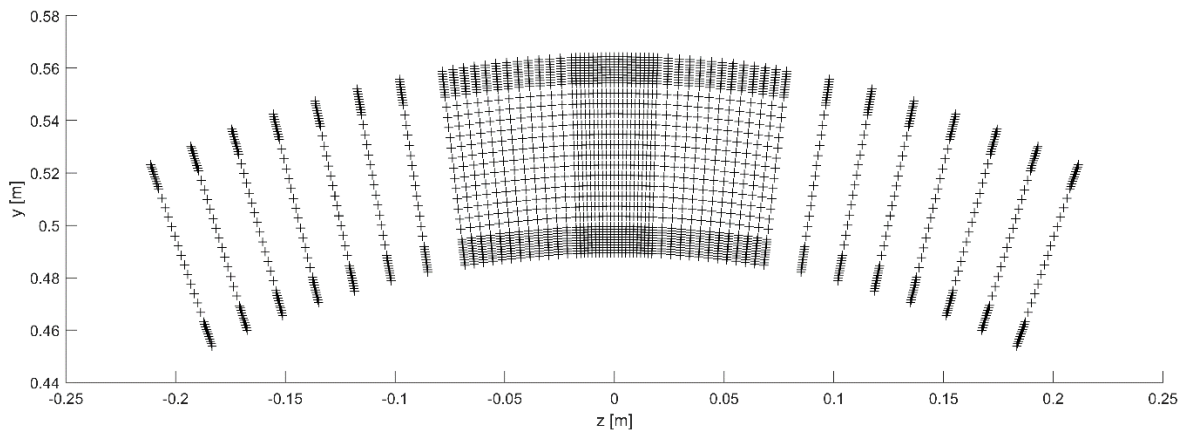

Figure 5-5 Mesh density at the OGV inlet.

The normalised total pressure distribution of the Kiel probe is shown in Figure 5-6. The area with a tangential resolution of 0.5 and below identifies the individual stator wakes from the upstream stator row and the boundary near the end-walls are resolved. As expected, in the area with a tangential resolution higher than 2°, no wakes can be identified.
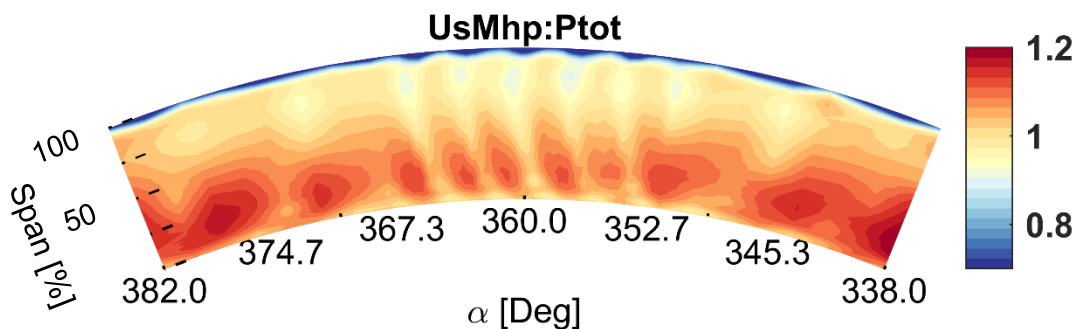
Figure 5-6 Normalised total pressure reading at the outlet of r2 by a Kiel probe over a 45 degree sector.

Figure 5-7 show the tangentially area averaged normalised total pressure at the rotor outlet when including different tangential resolutions of the full dataset. The blue line shows the average when the full sector is averaged, the red dashed line is the average for the 0.5-degree and black line for the 0.2-degree resolution. There is a 4% difference between the 2-degree sector and the 0.5 and 0.2-degree sector along most of the span. Near the shroud all sample areas show a good match. The sector of 0.2-degree and 0.5-degree resolution matches along the span as expect between 70%-85% of span, where the difference reaches a maximum of 1%. The Kiel probe data is presented between 3%-97% of the span. The probe diameter is 3% of the span and a safety margin of ~1.5% of span was utilised during testing to avoid the probe clashing with the endwall.
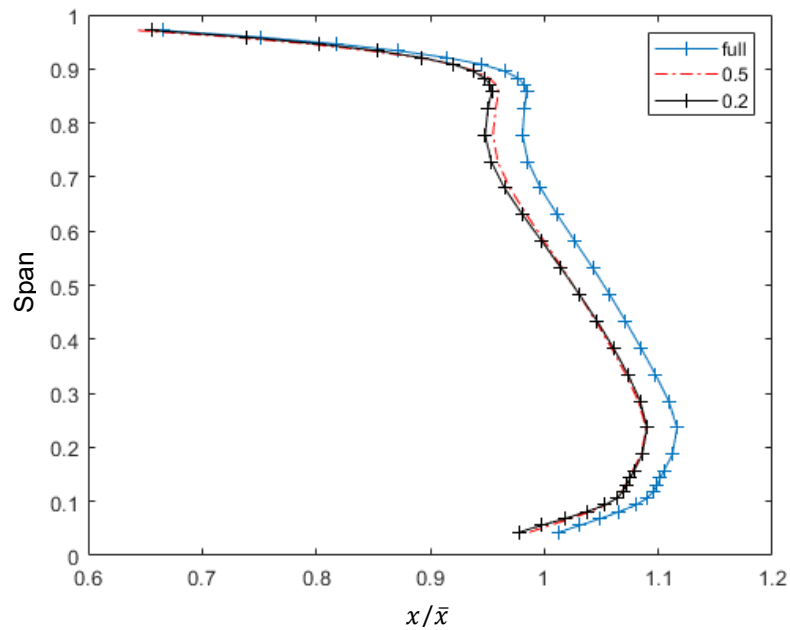
Figure 5-7 Normalised Kiel probe readings shown as radial profile for the full 45-degree sector (blue line), 16-degree sector (dashed red) and a 4-degree sector (black) at the OGV inlet.

The radial distribution of the normalised total pressure from a Kiel and MHP probe for the 0.5 sector is shown in Figure 5-8. One may note the offset in radial position due the slightly larger diameter of the MHP, which causes a slight increase in the endwall offset. In general, the MHP underpredicts the total pressure at the outlet of the compressor. The MHP overpredicts the total pressure at the last three points near the hub line. At these last data points the MHP is operating near the hub endwall in a highly gradient and fluctuating flow field. The results from the MHP are in line with expectation for a MHP in this type of operating conditions.
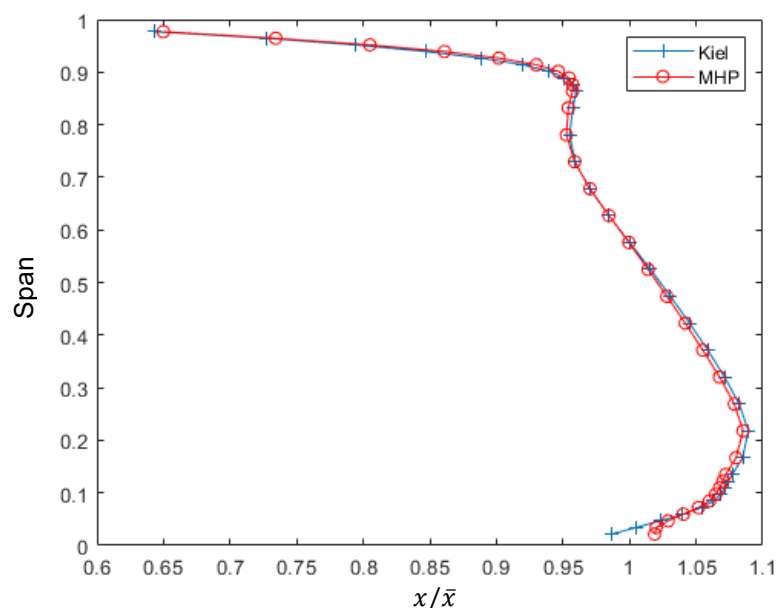

Figure 5-8 Normalised Kiel probe (blue) and MHP total pressure readings (red) shown as radial profile for the 16-degree sector at the OGV inlet.

The turbulence intensity was measured using hotwire anemometry, the velocity magnitude was measured with the MHP, and the temperature measured with the RTD at the outlet of the second rotor are shown together with the total pressure measured with the Kiel probe in Figure 5-9. The total pressure and velocity are normalised to emphasise similitude between turbulence, total pressure losses and velocity distribution. Near the shroud, the velocity, total pressure and turbulence intensity matches well and converges towards a single spanwise location. The settling time for the high sensitivity temperature sensor used at low speed is around 55 times longer than the pressure transducers. Hence, the temperature distribution in Figure 5-9 is known to be distorted. The investigation shown in Figure 5-9 was optimised for pressure readings and took roughly 3 hours to sample, the high-resolution sensor at a low-speed case would have require a full week.
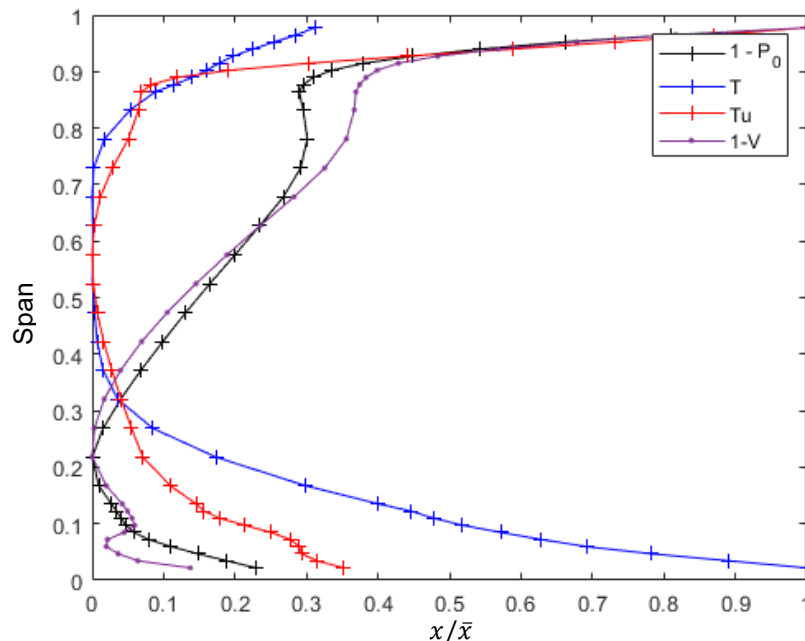

Figure 5-9 Radial distribution of properties obtained with the different instruments (Kiel, MHP, Hot-wire, temperature sensor) mounted at the inlet of the OGV (outlet of second rotor), see text for description.

Figure 5-10 shows the outlet of the rotor but only includes datapoints with a tangential resolution of 0.5-degree or smaller. In Figure 5-10, the wakes from the five upstream S1 stators are visible as lower total pressure areas. Physically, the S1 stator hub and shroud mount points are nearly radially positioned but one can note that the wakes are leaned with a larger tangential movement near the shroud. Effects from the rotor clearance can be identified as a lower pressure area where there is a noticeable interaction with each stator wake as a thickening of the shroud boundary layer. A portion of the boundary layer is not captured by the probe, but the last observed normalised total pressure is higher near the hub compared to the shroud. Below 12% of span, the wake from the upstream stator is thickened and gradually merges into the end-wall boundary layer.
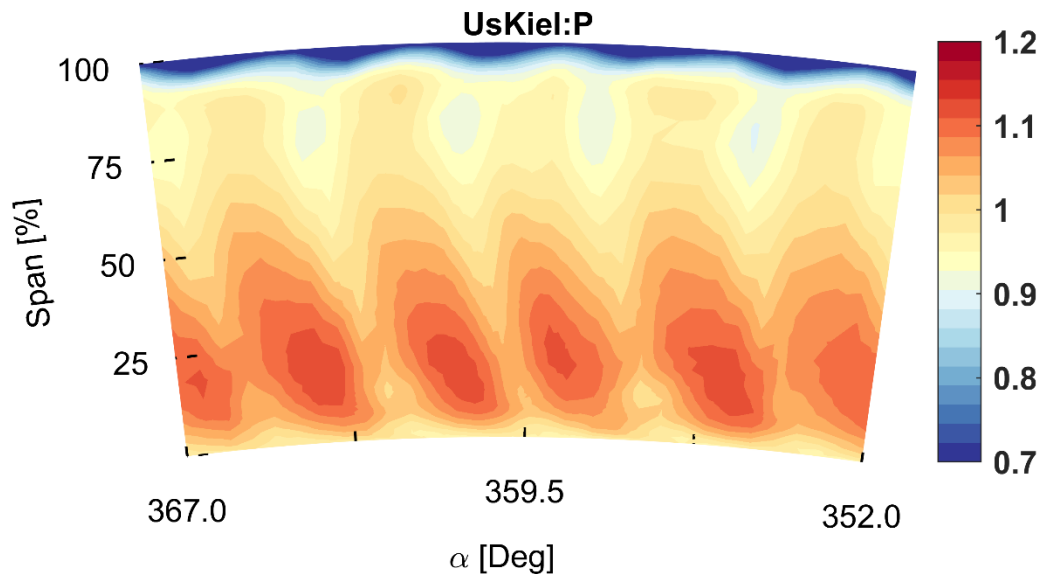
Figure 5-10 Normalized total pressure readings obtained with the Kiel probe in a sector of the OGV inlet (rotor 2 outlet) transversed with a resolution of 0.5-degrees or higher.

Figure 5-11 shown the normalised total pressure measured with MHP. As expected, the total pressure reading in the wakes are lower and peak total pressure is higher when compared to the Kiel probe. This has a limited effect for the tangentially averaged data but makes the wakes more profound in Figure 5-11 when compared to Figure 5-10. The probe is aligned with the flow and probe relative cone angle is never higher than 20-degree. Figure 5-12 show the velocity magnitude of the MHP readings. Velocity peaks at midspan is fluctuating with 5%. Below 7-8% of span the MHP is affected by the end-wall which can be seen as sharp non-physical changes in velocity. Note that the readings at the radial extremes have MHP ports far inside the boundary layer which is known to cause measurement offsets.
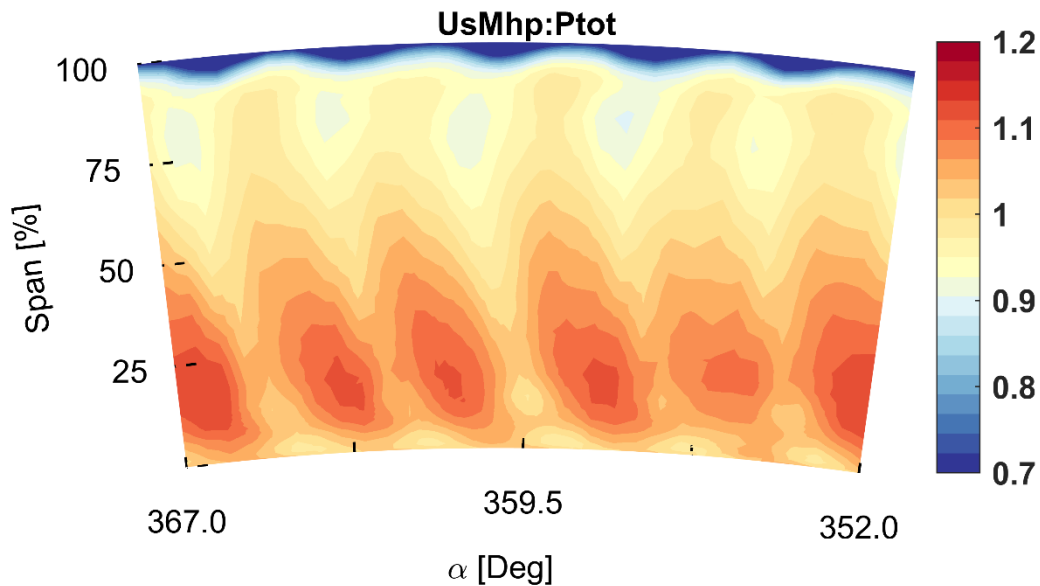

Figure 5-11. Normalized total pressure readings obtained with the MHP probe in a sector of the OGV inlet (rotor 2 outlet) transversed with a resolution of 0.5-degrees or higher.
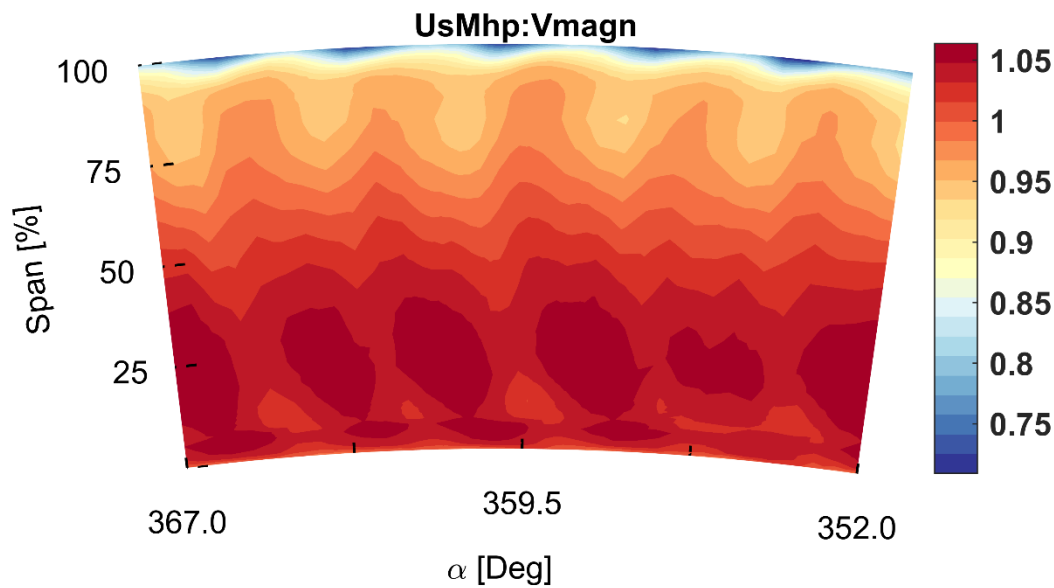
Figure 5-12 Normalized velocity readings obtained with the MHP probe in a sector of the OGV inlet (rotor 2 outlet) transversed with a resolution of 0.5-degrees or higher.

Figure 5-13 show the normalised intermittency where the S1 wakes can be identified by the increased intermittency. The intermittency is more profound inside the boundary layer near the end-wall but a progression of the intermittency from the end-wall along the trailing edge up to 20-30% of span can be observed. A boundary layer hot wire probe is primarily focused on fluctuation in the radial or axial direction and allows for detailed end-wall readings without high impact from rotor wakes. Wakes and turbulent structures in the tangential direction has a limited coverage.
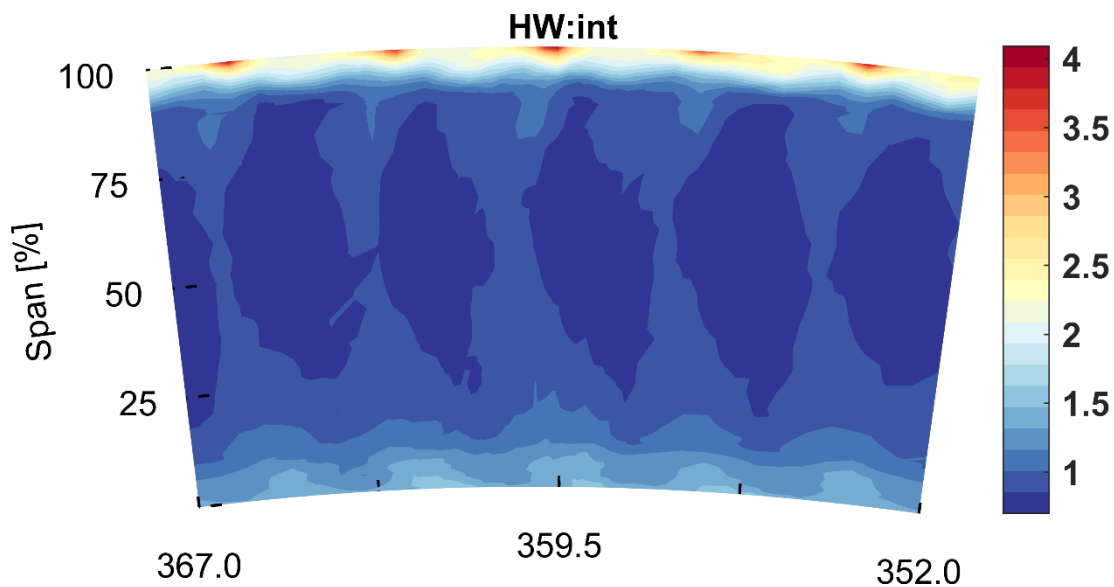

Figure 5-13 Normalized intermittency readings obtained with the hot wire anemometry in a sector of the OGV inlet (rotor 2 outlet) transversed with a resolution of 0.5-degrees or higher.

5.4 ICD-outlet plane measurements

Four sets of total pressure readings at midspan in a 45-degree sector at the outlet of the ICD are shown in Figure 5-14, with a tangential resolution of 0.5-degree. Three of these studies match the wake from the strut in terms of location and amplitude of total pressure losses. One may also notice that the total pressure is 5% higher near the strut compared to the middle of the section. The blue coloured total

pressure profile has a 5% lower normalised total pressure in the flow field between the struts. The blue line shows the strut located downstream of the inlet distortion identified in Figure 5-3 and Figure 5-4. This vane represented by the blue line is not utilised for detailed studies but is shown to illustrate the effect from the inlet distortion. There is no noticeable correlation between the OGV wakes and the total pressure reading at ICD outlet.
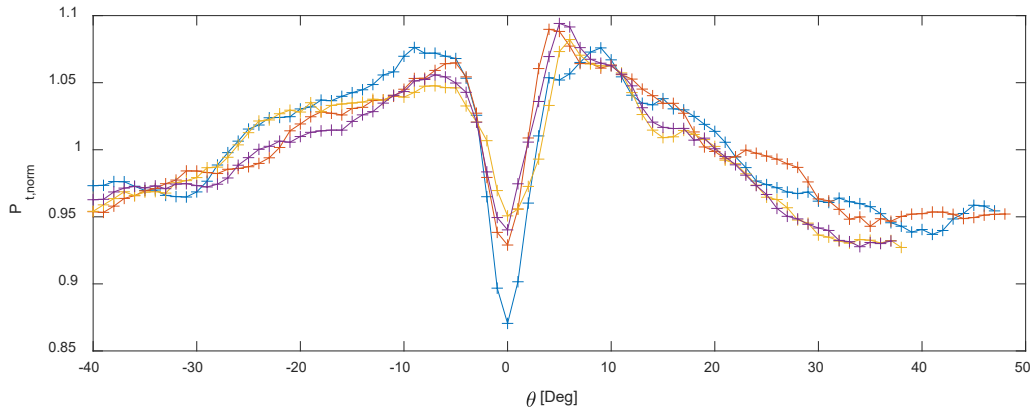

Figure 5-14 Total pressure readings at midpan of the ICD Outlet.

The ICD outlet plane has an identical mesh distribution as the studies at the rotor OGV inlet plane. In Figure 5-15 the normalized total pressure at the ICD outlet is shown. The strut wake is visible in the centre where the lowest total pressure losses are lower near the wall, especially along the hub. On each side of the strut at 25% and 40% of chord of the centrum are two low pressure areas. These are typically stream tubes expanded from the strut leading edge and during the deceleration near the hub during the radial turning. Note that the colormap and normalisation is local to emphasise flow features and is not identical to the inlet total pressure readings. There is a slight non-symmetry of the endwall boundary near the shroud which is likely caused by the differently instrumented and manufactured endplates. To the right in Figure 5-15 the shroud is vacuumed formed polycarbonate while the left is SLA printed and coated with NEXTEL. The two manufacturing methods have different geometrical tolerances and surface roughness which the experimental results indicate have an effect. Measurement during live testing shows that the vacuumed from window deform more than the thicker SLA printed window and hence the effective shroud line in this area is 0.5% larger near the shroud.
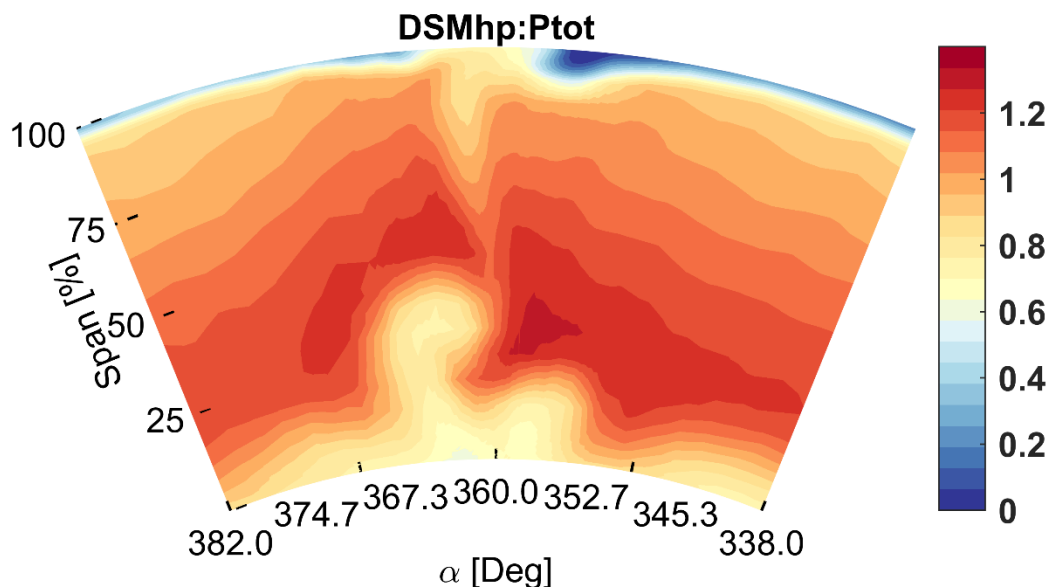

Figure 5-15 Normalised total pressure reading at the outlet of the ICD by a MHP over a 45-degree sector.

The radial distribution of the ICD provides qualitative insight of the radial redistribution of the normalised total pressure in the ICD. The tangentially average profile shows that the shroud boundary layer at 90% of span at the inlet is similar and no tangential redistribution has occurred.

5.5 Reynolds effects

Reynolds effects were investigated by selecting the ADP case but along the N0.75 speed line and compared with the reference case, namely APD N0.5. The normalised total pressure at the OGV inlet at N0.75 ADP is shown in Figure 5-16 where no substantial difference can be observed when compared to the same operational point but along the 0.5 speed line shown in Figure 5-10. As expected, the wakes are slightly more profound at the higher speed line.
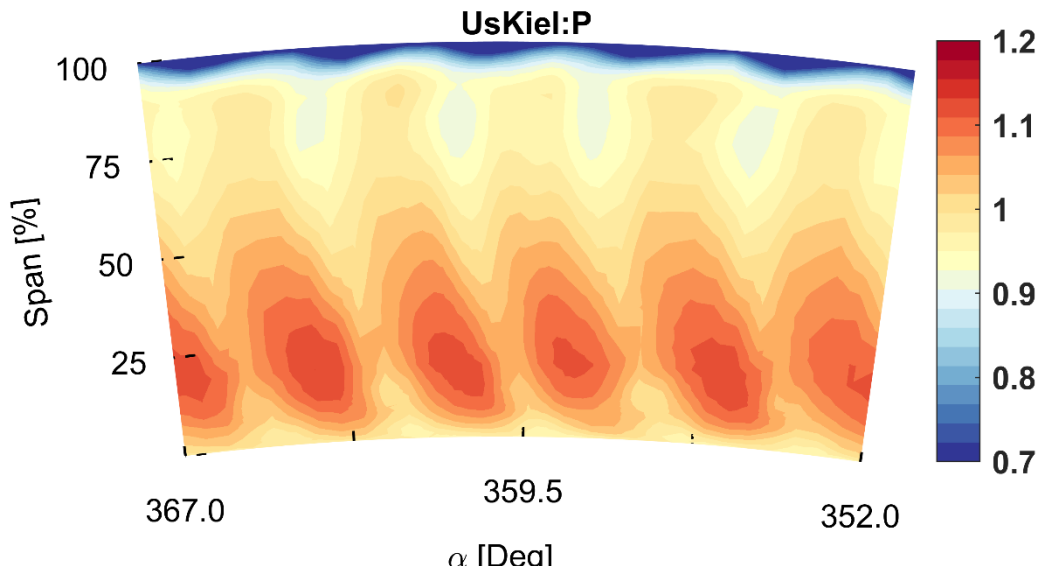

Figure 5-16 Sector of the OGV inlet (rotor 2 outlet) with resolution of 0.5 or higher showing the total pressure reading from the Kiel probe at 0.75 ADP.

Figure 5-17 show the normalised total pressure at the outlet of the ICD at ADP along the speed line N.075. The general flow field are similar to the earlier presented ADP at speed line N0.5. There is however a noticeable difference near the shroud when compared to Figure 5-14. The non-symmetry of the boundary layer has increased and is more profound with a thicker boundary on the left side of the strut compared to the right side. The secondary flow structures near the hub are similar in shape with the low Reynolds case having a more profound wake.
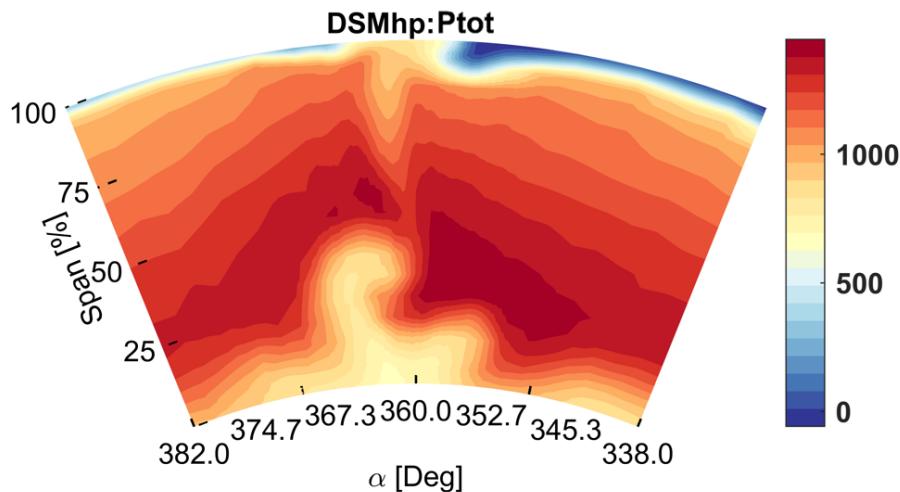

Figure 5-17 Normalised total pressure reading at the outlet of the ICD by a MHP over a 45-degree sector for ADP at speedline 0.75.

5.6 Off-design

An off-design operational point along the N0.5 speed line, but with an increased pressure ratio of 25% from ADP was selected to illustrate effects from operational changes. At higher pressure ratio each LPC stage load is increased, and one can notice wider radial wakes from the upstream stators and a shift in total pressure distribution from hub to shroud loaded which can be seen with higher total pressures in Figure 5-18. No large separation is visible even though the facility is operating near stall.
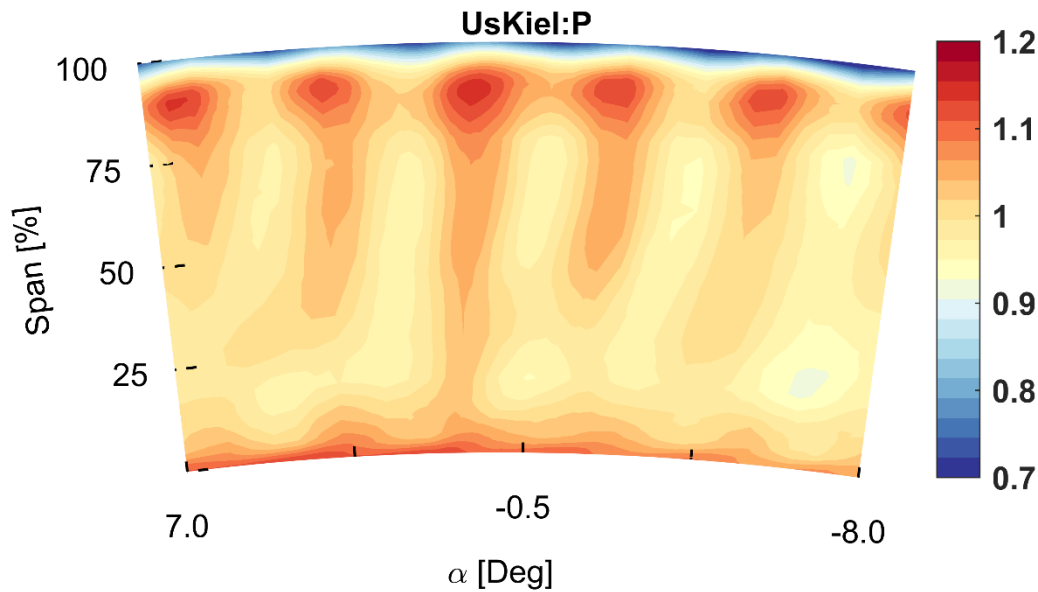

Figure 5-18 Sector of the OGV inlet with resolution of 0.5 or higher showing the total pressure reading from the Kiel probe at ADP + 25% in pressure ratio at speedline N0.5.

At the outlet of the LPC (Figure 5-19) the sturt wake and secondary flow structures are shifted tangentially. The non-uniformity near the shroud is less profound compared to the selected ADP case and the low pressure near the shroud is primarily visible near the strut. The outlet plane at high off-design angles are later in this report shown to be captured rather accurately by numerical simulations.
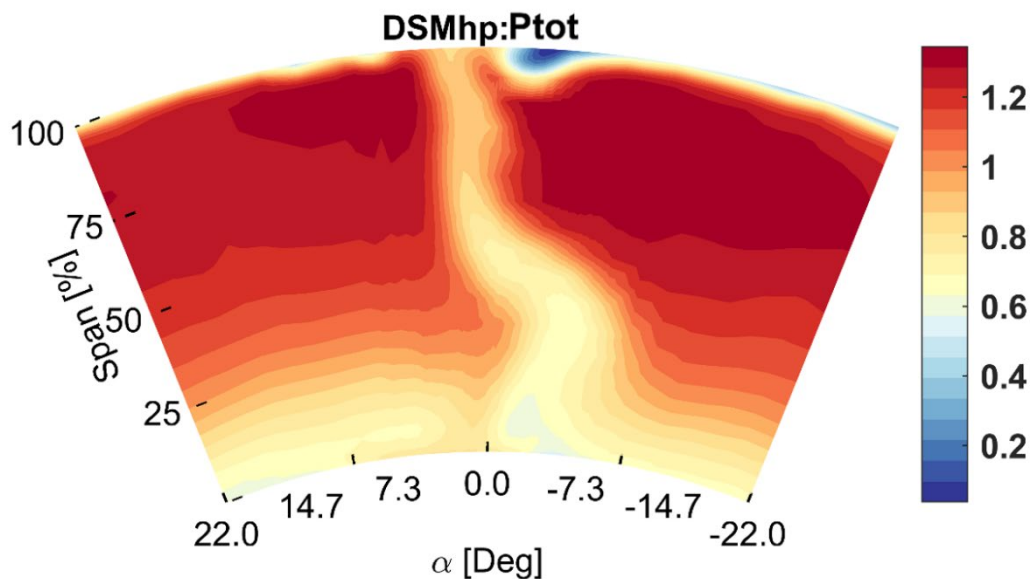

Figure 5-19 Normalised total pressure reading at the outlet of the ICD by a MHP over a 45-degree sector for 0.5 ADP + 25% in pressure ratio.

5.7 Heat management in the ICD

The heat transfer in the ICD is investigated by IR-thermography where a selected number of surfaces are heated. Figure 5-20 shows the normalised heat transfer on the hub line and strut for the ICD. The flow enters from the left and the unheated shroud has been cut off from the view to better visualise hub dependent features. The image consists of several views that have been patched without advanced normalisation between each sample point. The variation between each plane is therefore also a reflection on the stability of the measurement campaign. Individual streaks are visible from the upstream OGV stators along the hub line.
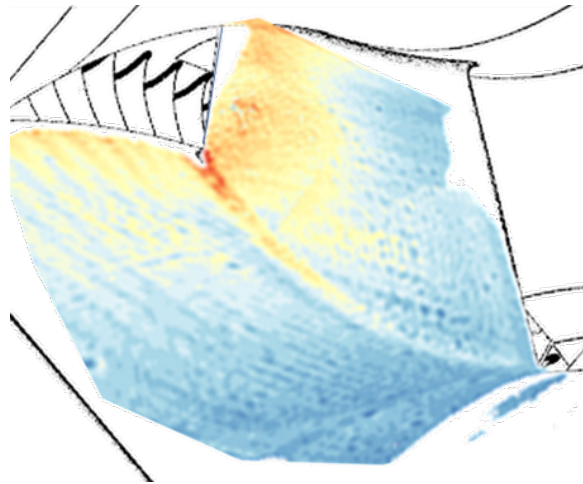

Figure 5-20 Normalised heat transfer in OGV-ICD domain using transient IR-thermography

6   Experimental verification of the numerical model

An image of the general flow field from the numerical simulation is shown Figure 6-1. The flow near the hub is illustrated by velocity streamlines coloured by velocity and dark streamlines along the strut show the fluid motion near surface of the strut. At the leading edge of the strut the low momentum boundary layer from near the hub from the LPC clashes with the strut hub interface and a rollup vortex is created. The flow simultaneously decelerates along the hub line and the stream tubes from the secondary flow structures are expanded. At the end of the strut the flow in the corner is separated and the stream tubes are no longer attached to the end-wall. This separation is known to be challenging to accurately predict using RANS simulations. The strut is not tangentially aerodynamically loaded and the flow entering the ICD has a low tangential velocity. Hence, the flow is virtually symmetrical around the strut in the tangential direction and two counter-rotating stream tubes exit the domain near the hub. Figure 6-1 does not provide any information near the shroud.
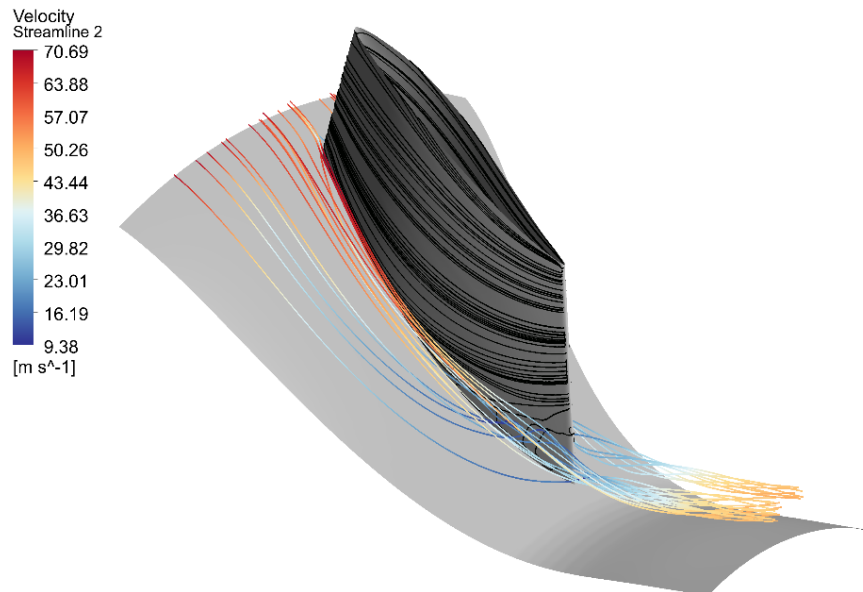

Figure 6-1 Streamlines on the ICD vane showing a hub separation and the two accompanying vortices being convected downstream.

6.1   Grid independence study

A mesh independence study (Table 6-1) has been carried out for the ICD with mesh cell counts ranging from 750 000 to 10 million cells and for the two transition models mentioned in section 4. A simulation of the complete ENABLEH2 compressor at the design operating point was performed beforehand to obtain profile data for setting the inlet boundary conditions for the ICD simulation. The inlet boundary condition featured a mass flow-averaged total pressure and temperature of 102021 Pa and 295 K while the average turbulence intensity was approximately 4.8%.

All meshes have a first node height below $y^+ = 1$ and were refined by setting a target mesh cell count in ANSYS Turbogrid, leading to global refinement in all directions of the mesh. For both transition models it was deemed that case 6 with 10 million cells was sufficiently accurate since it had normalized differences in the order of 1% relative to the second finest mesh. The pressure loss Δp_0 was calculated from the inlet to outlet, as was the total enthalpy change Δh_0. The heat flow q_{vane} was calculated as the area integral of the heat flux on the surface of the vane. It was observed that the total enthalpy change Δh_0 from inlet to outlet changed considerably from case 1 to 6, especially compared to the vane heat flow q_{vane}. The authors believe there are several factors contributing to this. The discrepancy between Δh_0 and q_{vane} is connected to overall convergence and the global domain imbalance of the energy equation. Numerical accuracy also plays a role in the global imbalance due to the small magnitude of heat transferred in the vane compared to the enthalpy flow in the inlet and outlets. The mesh study showed that a higher mesh resolution yielded better convergence and lower global imbalances, therefore Δh_0 approached the value of q_{vane} for the finer meshes. Both transition models showed similar convergence trends for the residuals, namely that the residual levels fell by at least three orders of magnitude and flattened out during the simulations. The largest domain imbalances found were for the

transition transport equations and were in the order of 0.02% for the finest mesh (case 6). The remaining domain imbalances were below this value and of similar levels for both transition models. There are also two hub separations on each side of the vane whose transient nature could potentially decrease convergence as seen in Figure 6-1.

Table 6-1 Results of the mesh independence study for the two analyzed transition models. The differences are relative to case 6 (Ref), the finest mesh

Gamma-Theta transition model

Case	N_{cells} $[10^6]$	Δp_0 [%]	Δh_0 [%]	q_{vane}[%]
1	0.75	9.5	23.16	1.04
2	1	7.25	18.57	0.68
3	2	3.89	8.72	0.29
4	5	1.15	3.35	0.15
5	7.5	0.57	1.11	0.1
6	10	Ref	Ref	Ref

Intermittency transition model

Case	N_{cells} $[10^6]$	Δp_0 [%]	Δh_0 [%]	q_{vane}[%]
1	0.75	9.1	23.22	1.03
2	1	8.72	19.57	0.7
3	2	4.48	9.46	0.24
4	5	0.85	2.88	0.12
5	7.5	0.63	0.9	0.04
6	10	Ref	Ref	Ref

Another interesting finding from the mesh study was that the onset and size of the transition region was mesh dependent, which resulted in the finer meshes having a delayed and prolonged transition region, as shown in Figure 6-2 for the Gamma-Theta model but was also present in the Intermittency model (not shown). Subsequent simulations were done using the 10 million cell mesh for both transition models since it was deemed adequate for representing the heat transfer in the flow.
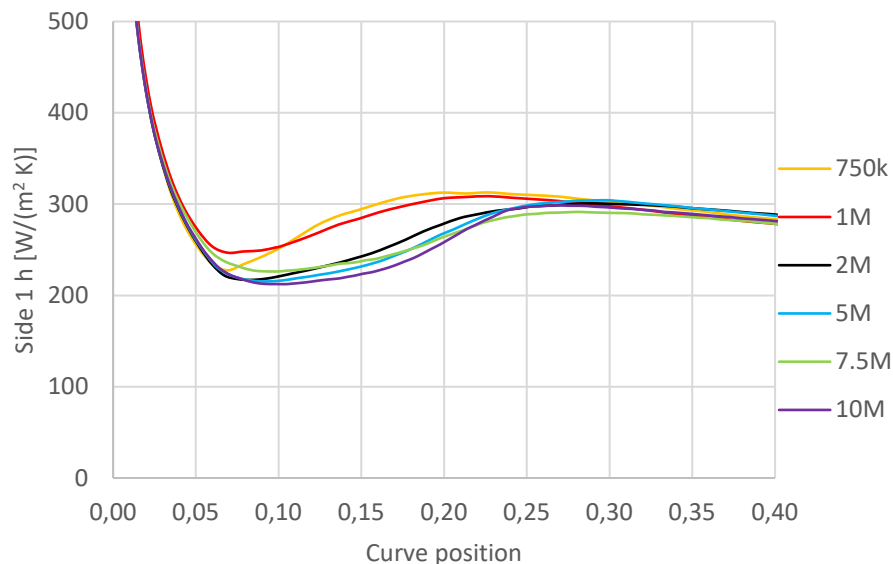

Figure 6-2 - Heat transfer coefficient h, at midspan for Side 1 of the ICD vane for the Gamma-Theta model for the different cases used in the mesh study. The curve position is 0 at the leading edge of the strut.

Transition from a laminar to a turbulent boundary layer is shown for the vane in Figure 6-3 in terms of turbulent kinetic energy and convective heat transfer coefficient. Both properties show that transition occurs at roughly the same location at approximately 20% of the chord position for these specific conditions.
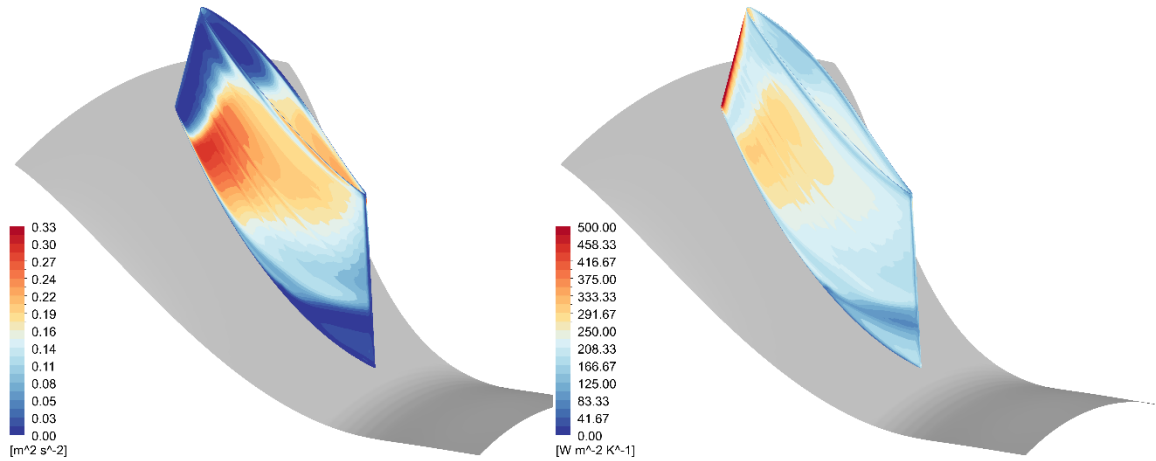
Figure 6-3 Turbulent kinetic energy on the vane surface (left) and convective heat transfer coefficient for the Gamma-Theta model (right). The value is capped at 500 [W/(m^2 K)] in order to improve readability, maximum value 900 [W/(m^2 K)] at the leading edge of the vane.

A parametric study of the effect of wall temperature on the transition location and heat transfer profile was carried out using both transition models. Heat transfer coefficients for these cases have been calculated for the ICD at midspan and are presented in Figure 6-4. Here it can be seen that both transition models yield very similar results and that the transition behaviour is similar between both models. The transition process seems to start further downstream (away from the leading edge) on the vane for decreasing wall temperature. This behaviour is difficult to discern graphically from the images alone, but the inflection points used for judging start and end of transition can be determined numerically and are presented in Table 6-1 and Table 6-2. This is in line with literature [37] on the effects of wall heat transfer on transition, namely that cooling acts to stabilize a boundary layer and increases its transition Reynolds number while heating is destabilizing and decreases the transition momentum thickness Reynolds number.
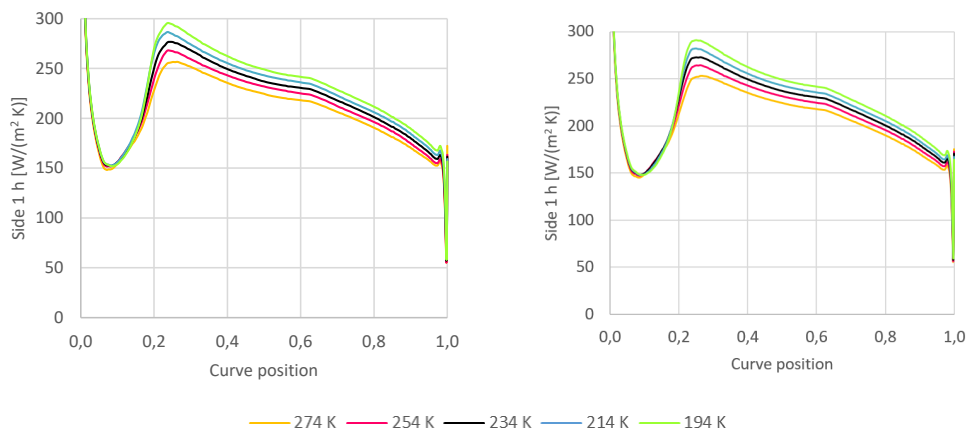

Figure 6-4 Heat transfer coefficient at midspan for for the Gamma-Theta(left) and Intermittency(right) model for a series of constant wall temperatures wall temperatures.

Table 6-2 Effect of wall temperature on onset and duration of transition for the Gamma-Theta model for midspan

Wall Temperature [K]	Start of transition	End of transition	Length of transition
274.7	0.0833	0.2631	0.1799
254.7	0.0833	0.2408	0.1575
234.7	0.0874	0.2408	0.1534
214.7	0.0874	0.2398	0.1524
194.7	0.0915	0.2398	0.1483

Table 6-3 Effect of wall temperature on onset and duration of transition for the Intermittency model for midspan.

Wall Temperature [K]	Start of transition	End of transition	Length of transition
274.7	0.0874	0.2688	0.1814
254.7	0.0874	0.2631	0.1758
234.7	0.0874	0.2631	0.1758
214.7	0.0915	0.2631	0.1717
194.7	0.0956	0.2631	0.1675

6.2 Comparison with experimental data

The present section targets the validation of the numerical model of the ICD with experimental data available from the experimental campaign. Data wascompared in terms of inlet radial profiles, chordwise pressure distributions, total pressure distributions at the outlet plane, and heat transfer data on the IGV-hub surfaces. The name convention of each case is identical to the result section.

6.2.1 OGV Inlet

The LPC was numerically modelled using mixing planes and all upstream rotor wakes were tangentially averaged out. Deviation at the OGV inlet could potentially have a large impact on the downstream OGV-ICD domain and hence the radial profiles are compared. Even with a perfect match with radial profiles there might still be local discrepancies between CFD and tests such as tangential variation and blade matching between OGV, ICD and LPC. Figure 6-5 shows a comparison of the radial profile of normalised total pressure at the inlet of the OGV. There is in general good agreement between the numerical simulation and the experimental results. From 90% of span and above the tangential averaged boundary layer build-up matches well with the experiments up to the last experimental point where the numerical average predicts a higher total pressure. From 40% of span and below the radial profile is nearly spot on with only minor variation. Between the 40-80% of span the numerical simulation predicts a higher total pressure while a lower pressure near between 80 and 90% of span.
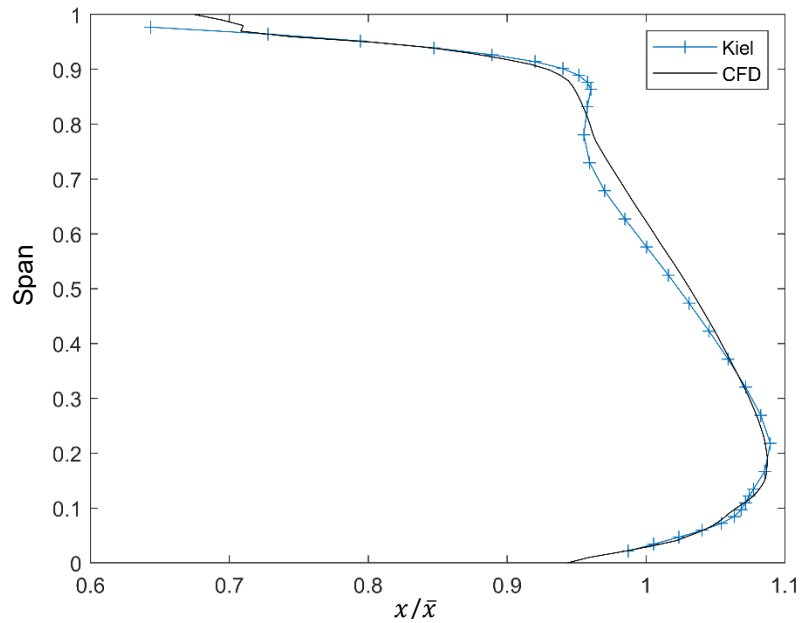
Figure 6-5 Normalised total pressure at the inlet of the OGV for Keil probe measurements and numerical simulations

Figure 6-6 shows the dynamic pressure at the inlet to the OGV of the numerical simulations in black and readings from the MHP in blue. The general trends between the experimental data are acceptable considering a potential interference in the MHP data from pressure gradients and angle fluctuations.
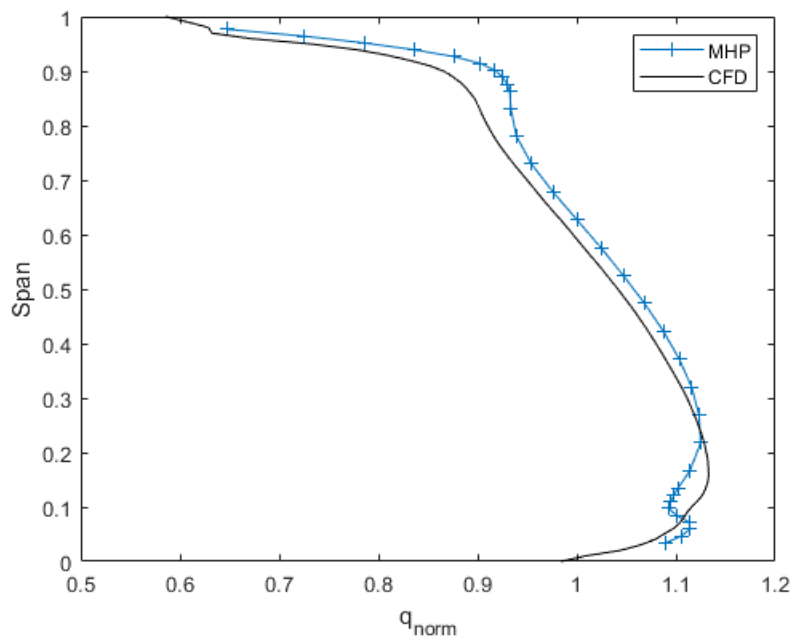

Figure 6-6 Radial velocity component form MHP measurements and CFD

6.2.2 Blade Loading

Figure 6-7 compares the pressure distribution on the OGV, instrumented with pressure taps at midspan, with the numerical simulations at design conditions. The numerical simulation was carried out using the experimental operational conditions and the data is shown as a solid red line. The blade loading is satisfactorily matches the current numerical model of the LPC.
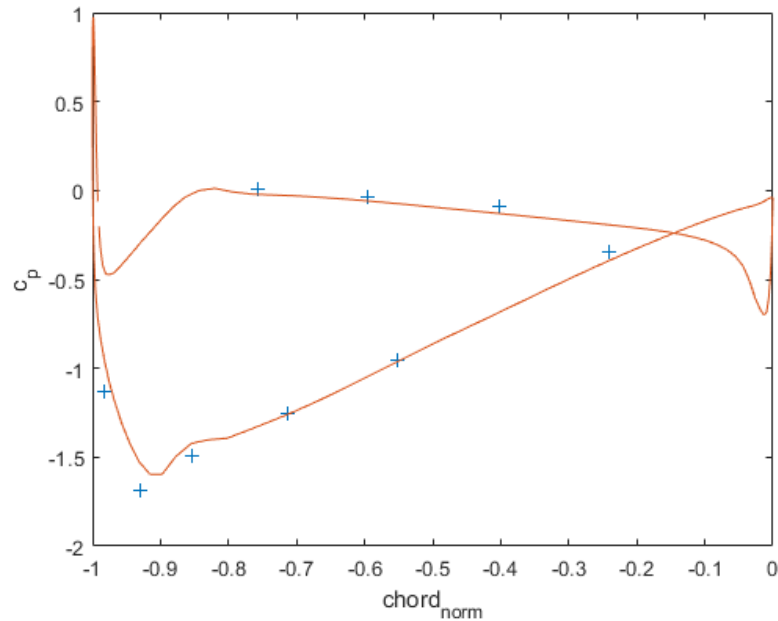
Figure 6-7 Blade loading at midspan for an OGV.

6.2.3 ICD outlet

A comparison between the normalised total pressure contours at the ICD outlet at 0.5 ADP is shown in Figure 6-8, the numerical results are shown to the left and the experimental data to the right. There are general agreements between the numerical and experimental result at the outlet of the ICD. The relative hub/strut separation are of similar magnitude and the stream tube expansion on each side of the strut is similar with a slightly larger expansion on the left side. However, the numerical results indicate that the hub/strut separation is fully detached from the end wall, i. e. both hub/strut separation is no longer attached to the end wall. The experimental data indicate a semi-attached flow. In the experimental data the right side is still attached to the hub while the left corner separation has been stretched out along the strut trailing edge. Near the shroud (above 90% of span) there is a low momentum flow whose distribution is similar to the experimental results, with a slight downward distribution where the strut interacts with the shroud boundary layer.
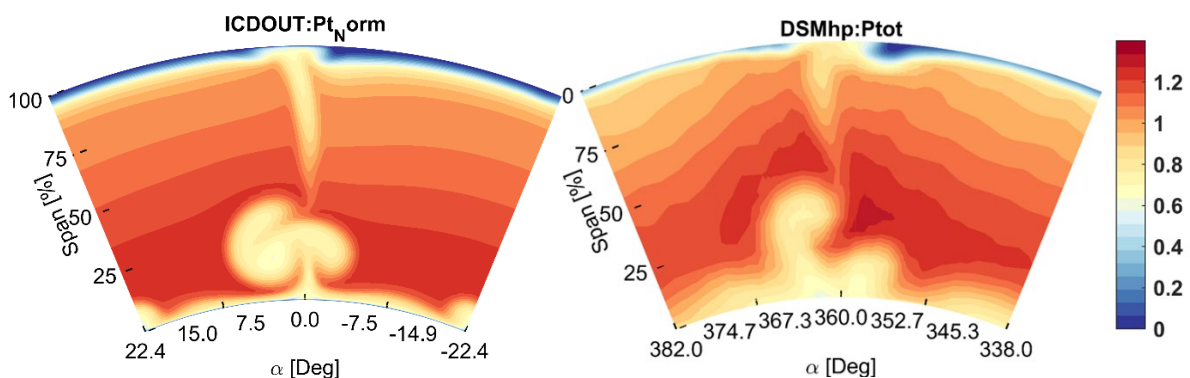

Figure 6-8 Normalised total pressure contours at the outlet plane at N0.5 ADP: numerical simulation (left) and experimental data (right).

The normalised total pressure at the off-design (pressure ratio +25%) for the numerical case is shown on the left in Figure 6-9 while the experimental results are shown to the right. The numerical results are in general good agreement with the experimental data. The overall distribution of the ICD strut wake is similar with the exception near the hub. In the numerical results, the secondary flow structures from the hub/sturt are found at a higher radial position compared to the experimental result. This indicates that a separation along the hub occurs in the numerical domain but does not occur in the experimental data.

Near the shroud, the numerical results overpredict the boundary layer thickness but the stator/shroud interaction is predicted correctly.
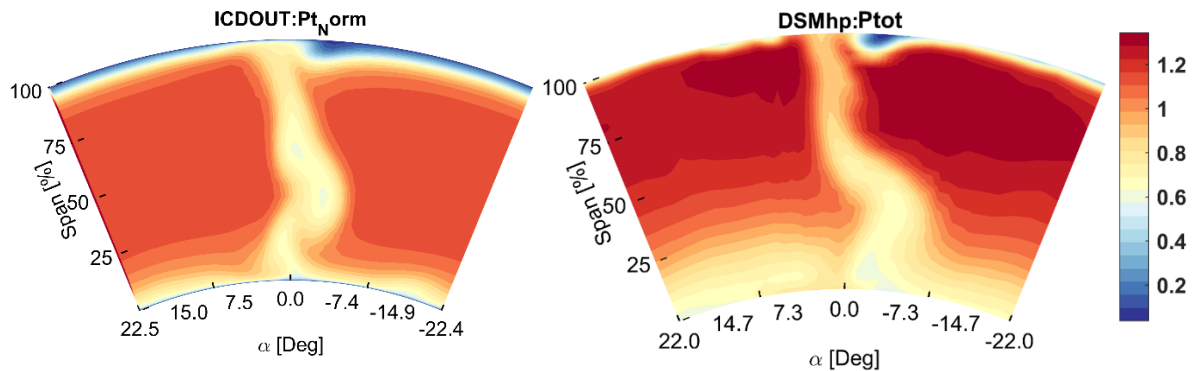

Figure 6-9 Normalised total pressure contours for the operational conditions ADP+0.05 N0.5 at the outlet: numerical simulation (left) and experimental data (right).

6.2.4   Laminar-turbulent Transition and heat transfer in the ICD

The laminar-turbulent behaviour of the numerical and experimental data is evaluated by studying the normalised heat transfer coefficient distribution on the strut in the ICD. Figure 6-10 shows the computed normalised heat transfer coefficient (left) and the experimental results (right). The numerical simulation predicts a laminar-turbulent transition around 0.2 of the chord which can be seen as a low heat transfer area followed by a rapid increase in heat transfer. In the numerical results there is an area of low heat transfer rate near the trailing edge and hub which is in line with a separated secondary flow structures seen in Figure 6-8. The numerical results also show a decline in the strut heat transfer in the vicinity of the shroud. The experimental dataset is constructed from five different datasets that has been overlapped in Matlab and superimposed on an image from a render of the CAD with the same viewpoint. In the experimental dataset the wakes from the upstream OGVs are clearly visible as streaks of low heat transfer rate which are decaying throughout the domain. Following the same rationale as for the numerical data there is no clear indication of where a laminar-turbulent transition occurring in the available experimental data. However, the whole strut is not visible, and it is likely that the transition occurs further upstream and that what is visible is the turbulent boundary layer growth. The heat transfer coefficient downstream of the laminar-turbulent transition in the numerical results matches the experimental observation. In the experimental data there is no clear indication for a corner separation at the hub near the trailing edge of the strut. Noteworthy was that a small variation in ambient conditions during the facility operation had a large effect on the measured heat transfer rate in the visible range on the strut.
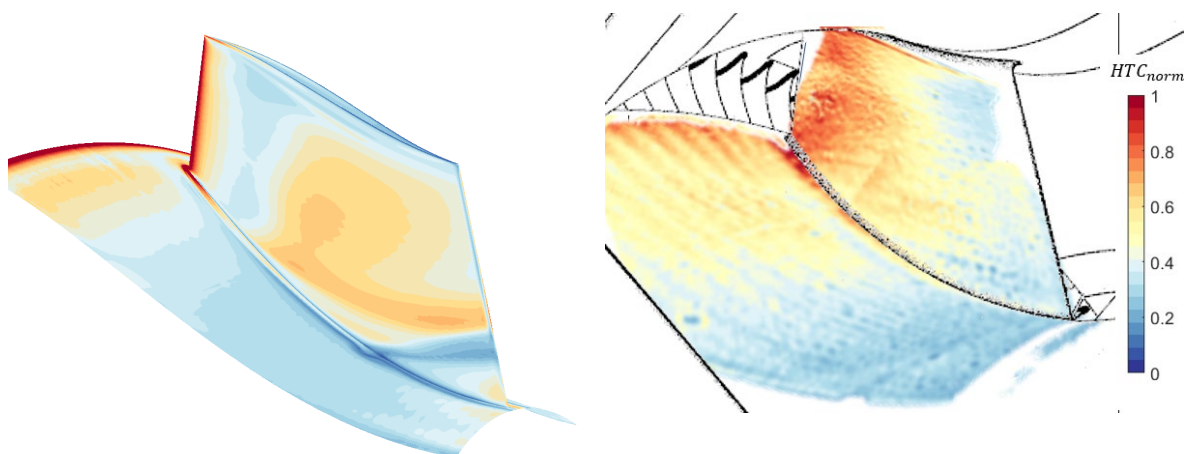

Figure 6-10 Normalised heat transfer coefficient distribution for the strut and the hub surface for the APD case at N.05. The numerical results are shown on the left and experimental results from several merged datasets are superimposed on a rendering of the facility on the right.

7 Conclusions

This report provides a detailed description of the design, construction and commissioning of the newly constructed low-pressure compressor test facility as part of the ENABLEH2 project. The report also presents key performance indicators and aerothermal experimental results from an OGV-ICD investigation. Detailed numerical investigations of the OGV and ICD performance are included to describe the approach and methods implemented to derive the numerical database that attempts to match the experimental results. The facility's performance and experimental verification data exceeds the expected quality targets with exceedingly high stability, flow uniformity, and resolution.

The design section of this report presents several risk mitigations to avoid unwanted flow features or effects in the operational range of the facility. However, there are always unknown features and uncertainties in the design work. The experimental results were used to verify several design choices by investigating flow features downstream the LPC outlet. An operation point at the lowest speed line was selected to evaluate the stability and capabilities of the facility. At these conditions, instabilities in machinery (such as motor power input) or uncertainties in measurement should be at the highest level.

The results in this report do not identify any large-scale performance variations, where most monitoring values fluctuated within 0.02% or less during a near 3-hour long operation. Figure 5-1 and Figure 5-2 show the compressor variation of key monitoring parameters where RPM fluctuates less than 0.1RPM. The low fluctuation verifies that the large-scale system control of the facility, such as cooling system, or motor controller provides ample stability for detailed studies even at less than a tenth of the design load and that normalisation work is expected to be satisfactory.

The facility outlet uniformity was evaluated by traversing a 330-degree sector at midspan. The study found variations of total pressure around 1%, which strongly indicates that the compact volute, the conditioning system and the LPC are all working as expected. There is few instances where the fluctuation reaches 1.5% which requires further investigation, but there are several reasonable explanations for a local deviation at the ICD inlet. Moreover, a separation in the volute or misalignment during assembly would instead cause large scale variations and not a localized one at about 180-degrees. One probable reason for this deviation is a large temperature probe located at the inlet but there are several other likely contributors. The current mitigation method of avoiding studies in the sector is for the moment satisfactory.

The required traverse resolution to perform a plane investigation has been evaluated in the pre-test evaluation and during the experimental campaign. Current datasets motivate a tangential resolution on the OGV inlet between 0.2 and 0.5-degrees to capture plane properties accurately. The minimal probe size currently limits the measurement of the whole end wall flows but a tangential resolution of 37 points is for the current studies deemed satisfactory.

Regarding numerical model validation, it was observed that the experimental data is well matched at the inlet of the OGV. Computed tangentially averaged profiles of normalised total pressure and dynamic pressure are compared with experiments and in general show a very good agreement. Furthermore, the blade loading of the OGV at midspan matches well with the experimental pressure taps. The matching of tangentially averaged profiles and blade loading indicate that the simulation captures the general flow field in the LPC at design conditions. Note that the stall behaviour, blade matching and similar effects have not yet been investigated and that substantially more intricate numerical and experimental studies are required to study these in detail.

Reynolds number dependent flow features are difficult to predict at an early design stage and every facility is unique. Hence there was a risk that the operational point in the designed operational space could have large scale performance deterioration due to Reynolds dependent features. Features of special concern revolved around laminar separation on stators, on rotor blades or large corner separation propagating into the ICD test section at lower design speeds. No large-scale unexpected performance deterioration has been identified from the current investigations at the OGV Inlet and ICD outlet presented in this report. Experimental data have shown higher robustness to stall and separation when compared to the present numerical simulations. Changes in Reynolds number produced the expected effect in stator wake thickness and changes to end-wall boundary layer thickness. Noteworthy

is that the increased pressure ratio at higher rotational speeds changes the tip leakage behaviour but the authors find it unlikely to have as root cause Reynolds dependent features, and therefore is more likely due to the increased tip loading.

One target of this report was to provide a validation database for heat-transfer on turbomachinery surfaces in axial compressors, for the purpose of intercooling on future LH_2 fuelled applications. Heat exchange while using existing surfaces allows for exchanging heat between the core and the cryogenic fuel without incurring an additional heat-transfer related pressure loss. To fully assess the aerothermal performance of such surfaces in an axial compressor, detailed numerical and experimental heat-transfer studies were carried out in the interconnecting compressor duct (ICD).

Two different CFD transition models, the Gamma-Theta and Intermittency models, were used to simulate transition in the ICD. A mesh independence study was carried out which showed that a well-refined mesh was needed to reach good convergence, which was especially challenging considering the relatively small amount of heat transferred in the vane compared to the enthalpy flow in the inlet and outlets. It was also seen that the onset and size of the transition region was highly mesh dependent, resulting in the finer meshes having a delayed and prolonged transition region compared to the rough meshes.

A parametric study was carried out where the wall temperature was varied to see the effect of increased cooling on transition. It was seen that for decreasing wall temperature the onset of transition moved further downstream, and the length of the transition zone decreased, of which the former is supported by literature. Overall, the two transition models yielded very similar results, especially regarding the heat transfer coefficient at the vane.

The numerical results from the ICD simulations agree with experimental observations and the numerical tools selected capture the sought physics. There are some minor discrepancies in the dataset which require further studies to be resolved or considered during design. The secondary flow structures that occur on each side of the strut are, in the numerical results, seen to fully separate from the hub and located symmetrical around the strut trailing edge. In the experimental data the hub/strut secondary flow structures are non-symmetric with one attached to the hub end-wall and one further distributed radially into the flow. The are several cases of OGV interaction with struts in the literature and the author expects this to be the case as well. For a numerical simulation with a radial profile with low tangential velocity at the inlet of the ICD, the results should be near symmetrical. Why this is not observed in the experimental results is likely due to wake interaction with either, OGV, stator wakes, or both. Future work is likely required to consider OGV matching and to utilise more advanced inlet conditions where stator and OGV wakes from experimental data are included in the numerical simulations. However, from current data, the stator wakes from the OGV decays relatively rapidly throughout the ICD. Heat transfer studies cannot detect any stator wakes downstream 0.5 of ICD-strut chord and there is no detection of the OGV presence in the outlet of the ICD.

8 Bibliography

[1] M. Lejon, T. Grönstedt, N. Glodic, P. Genrup and A. Mann, "Multidisciplinary Design of a Three Stage High Speed Booster," in *Turbo Expo: Power for Land, Sea, and Air*, Charlotte, North Carolina, 2017.

[2] J. P. Longley, "Measured and Predicted Effects of Inlet Distortion on Axial Compressors," in *Turbo Expo: Power for Land, Sea, and Air*, 1990.

[3] I. Jonsson, G. Debarshee and C. G. T. Xisto, "Design of Chalmers new Low-pressure Compressor Test Facility for Low-speed testing of Cryo-Engine Applications," Gdansk, 2021.

[4] A. Schaffler, "Experimental and Analytical Investigation of the Effects of Reynolds Number and Blade Surface Roughness on Multistage Axial Flow Compressors," *Journal of Engineering for Power,* vol. 102, no. 1, pp. 5-12, 01 1980.

[5] A. Carter, G. Annear, G. Green and C. Moss, The effect of Reynolds number on the performance of a single-stage compressor, Ministry of Aviation, Aeronautical Research Council, 1957.

[6] R. E. Mayle, "The 1991 IGTI Scholar Lecture: The Role of Laminar-Turbulent Transition in Gas Turbine Engines," *Journal of Turbomachinery,* vol. 113, no. 4, pp. 509-536, 10 1991.

[7] T. R. Camp and H.-W. Shin, "Turbulence Intensity and Length Scale Measurements in Multistage Compressors," *Journal of Turbomachinery,* vol. 117, no. 1, pp. 38-46, 01 1995.

[8] H. P. Grant, "Turbulence characteristics of compressor discharge flows. JT9D engine tests," in *NASA. Lewis Res. Center Premixed Prevaporized Combustor Technol. Forum*, 1979.

[9] H. Youngren and M. Drela, "Viscous inviscid method for preliminary design of transonic cascades," in *27th Joint Propulsion Conference*, 1991.

[10] B. J. Abu-Ghannam and R. Shaw, "Natural Transition of Boundary Layers—The Effects of Turbulence, Pressure Gradient, and Flow History," *Journal of Mechanical Engineering Science,* vol. 22, no. 5, pp. 213-228, 1980.

[11] H. Schreiber, W. Steinert and B. Kusters, "Effects of Reynolds Number and Free-Stream Turbulence on Boundary Layer Transition in a Compressor Cascade," *Journal of Turbomachinery,* vol. 124, no. 1, pp. 1-9, 02 2000.

[12] J. Groth and A. V. Johansson, "Turbulence reduction by screens," *Journal of Fluid Mechanics,* vol. 197, pp. 139-155, 1988.

[13] V. Cyrus, "An Experimental Study of Stall in Four Axial Compressor Stages," in *Turbo Expo Power for Land, Sea, and Air*, 2000.

[14] International Organization for Standardization, ISO, "Geometrical Product Specifications (GPS) — Surface texture, 4287," 1997.

[15] I. Jonsson, V. Chernoray and R. Dhanasegaran, "Infrared Thermography Investigation of Heat Transfer on Outlet Guide vanes in a Turbine Rear Structure," vol. 5, no. 23, 2020.

[16] K. A. Flack and M. P. Schultz, "Review of Hydraulic Roughness Scales in the Fully Rough Regime," *Journal of Fluids Engineering,* vol. 132, no. 4, 04 2010.

[17] W. C. Swan, "A Practical Method of Predicting Transonic-Compressor Performance," *Journal of Engineering for Power,* vol. 83, no. 3, pp. 322-330, 07 1961.

[18] C. C. Koch, "Stalling Pressure Rise Capability of Axial Flow Compressor Stages," *Journal of Engineering for Power,* vol. 103, no. 4, pp. 645-656, 10 1981.

[19] J. D. Denton, "Some Limitations of Turbomachinery CFD," in *Turbo Expo: Power for Land, Sea, and Air*, 2010.

[20] C. Wang, J. Hu, J. Li and Zhiqiang, "Three-dimensional compressor blading design improvements in low-speed model testing," *Aerospace Science and Technology,* vol. 63, pp. 179-190, 2017.

[21] D. C. Wisler, "Loss Reduction in Axial-Flow Compressors Through Low-Speed Model Testing," *Journal of Engineering for Gas Turbines and Power,* vol. 107, no. 2, pp. 354-363, 04 1985.

[22] J. D. Denton, "The 1993 IGTI Scholar Lecture: Loss Mechanisms in Turbomachines," *Journal of Turbomachinery,* vol. 115, no. 4, pp. 621-656, 10 1993.

[23] S. Sakulkaew, C. S. Tan, E. Donahoo, C. Cornelius and M. Montgomery, "Compressor efficiency variation with rotor tip gap from vanishing to large clearance," *Journal of turbomachinery,* vol. 135, no. 3, 2013.

[24] L. Ellbrant, L.-E. Eriksson and H. Mårtensson, "Predictive Capability of CFD Models for Transonic Compressor Design," in *Turbo Expo. Power for Land, Sea, and Air*, 2014.

[25] I. Jonsson, C. Xisto, M. Lejon, A. Dahl and T. Grönstedt, "Design and Pre-Test Evaluation of a Low-Pressure Compressor Test Facility for Cryogenic Hydrogen," in *AMSE Turbo Expo 2020*, Online, 2021.

[26] C. Ortiz Duen~as, R. J. Miller, H. P. Hodson and J. P. Longley, "Effect of Length on Compressor Inter-Stage Duct Performance," in *Turbo Expo: Power for Land, Sea, and Air*, 2007.

[27] E. M. J. Naylor, C. O. Dueñas, R. J. Miller and H. P. Hodson, "Optimization of Nonaxisymmetric Endwalls in Compressor S-Shaped Ducts," *Journal of Turbomachinery,* vol. 132, no. 1, 09 2009.

[28] A. D. Walker, A. G. Barker, J. F. Carrotte, J. J. Bolger and M. J. Green, "Integrated Outlet Guide Vane Design for an Aggressive S-Shaped Compressor Transition Duct," *Journal of Turbomachinery,* vol. 135, no. 1, 10 2012.

[29] D. Walker, F. Wallin, R. Bergstedt and G. Peacock, "Aerodesign and validation of turning struts for an intermediate compressor duct," 2015.

[30] I. Jonsson and V. R. B. Chernoray, "Surface Roughness Impact On Secondary Flow and Losses in a Turbine Exhaust Casing," Olso, 2018.

[31] I. D. S. Jonsson, V. Chernoray, O. L. Thulin and Jonas, "Experimental and Numerical Study of Laminar-Turbulent Transision on a Low-Pressure Turbine Outlet Guide Vane," vol. 143, 2021.

[32] B. Rojo, "Aerothermal Experimental Investigation of LPT-OGVs," Gothenburg, 2017.

[33] E. W. Lemmon, L. H. Marcia, M. O. McLinden and I. Bell, "NIST reference fluid thermodynamic and transport properties–REFPROP," NIST standard reference database 23 (2002): v7, 2002.

[34] ANSYS, *ANSYS CFX-Solver Modelling Guide,* version 2021r1: ANSYS Inc., 2022.

[35] R. Langtry and F. Menter, "Transition modeling for general CFD applications in aeronautics.," in *In 43rd AIAA aerospace sciences meeting and exhibit*, Nevada, 2005.

[36] F. R. Menter, P. E. Smirnov, T. Liu and A. Ravikanth, "A one-equation local correlation-based transition model.," in *Flow, Turbulence and Combustion 95, no. 4 : 583-619*, 2015.

[37] H. Schlichting and K. Gersten, Boundary-layer theory, Springer Science & Business Media, 2003..

[38] S. Deshpande, I. Jonsson and V. Chernoray, "Effect of Surface Roughness on Aerodynamic Performance Of Turbine Rear Structure," Phoenix, 2019.

ENABLEH2

Public Report

Core flow cooling rig design and CFD database report

Authors

Isak Jonsson, Alexandre Capitao Patrao, Carlos Xisto

Chalmers University